Fall 2019

The Variability of High-Frequency Motions and Their Interactions with the Mesoscale on the Mississippi Shelf

Jordan Earls
University of Southern Mississippi

THE VARIABILITY OF HIGH-FREQUENCY MOTIONS AND THEIR

INTERACTIONS WITH THE MESOSCALE ON THE MISSISSIPPI SHELF

by

Jordan Joseph Earls

A Thesis
Submitted to the Graduate School,
the College of Arts and Sciences
and the School of Ocean Science and Engineering
at The University of Southern Mississippi
in Partial Fulfillment of the Requirements
for the Degree of Master of Science

Approved by:

Dr. Maarten C. Buijsman, Committee Chair
Dr. Stephan D. Howden
Dr. Davin J. Wallace

_____ _____ _____
Dr. Maarten C. Buijsman   Dr. Jerry D. Wiggert   Dr. Karen S. Coats
Committee Chair   Director of School   Dean of the Graduate School

December 2019

THE UNIVERSITY OF
SOUTHERN
MISSISSIPPI.

ABSTRACT

In this study, we examine the spatial and temporal variability of high-frequency and low-frequency motions across the Mississippi Shelf and how the high-frequency motions are modulated by low-frequency mesoscale motions. For this purpose, we use Acoustic Doppler Current Profiler (ADCP) measurements collected at nearshore (23 m), mid-shelf (60 m), and shelf break (88 m) stations. High-frequency motions are defined as motions with periods less than 36 hours, whereas mesoscale motions have larger periods. The collected datasets are analyzed through bandpass filtering, least square harmonic analysis, spectral analysis, and empirical orthogonal functions (EOF). We find that along-shelf barotropic mesoscale motions contain the most energy. While weak barotropic tidal motions are present, near-inertial motions with diurnal frequencies constitute a significant fraction of the high-frequency motions. In shallow water, the wind-induced near-inertial motions are found to be suppressed by low-frequency downwelling that destroys or subdues the water column stratification. However, the correlation between mesoscale processes and high-frequency motions is not found at the mid-shelf and shelf break stations.

ACKNOWLEDGMENTS

TABLE OF CONTENTS

LIST OF TABLES

LIST OF ILLUSTRATIONS

LIST OF ABBREVIATIONS

ADCP	Acoustic Doppler Current Profiler
CTD	Conductivity, Temperature, Density Instrument
DISL	Dauphine Island Sea Lab
EOF	Empirical Orthogonal Functions
FFT	Fast Fourier Transformation
KE	Kinetic Energy
mab	Meters above bottom
NaN	Not a Number
NDBC	National Data Buoy Station
NIW	Near-inertial Wave
NOAA	National Oceanographic and Atmospheric Administration
SEED	Shelf Energetics and Exchange Dynamics Project
ST	Station
USM	The University of Southern Mississippi

CHAPTER I – INTRODUCTION AND BACKGROUND

The overall objective of this research project will be to study low and high-frequency motions and how they vary across the Mississippi Shelf. The specific goals of this study are to determine what motions are dominant across the Mississippi Shelf and how the mesoscale motions and high-frequency motions interact with each other on the shelf.

1.1 Study Area

The Mississippi Shelf is a long, shallow sloping shelf that extends to over 200 kilometers offshore in the Gulf of Mexico west of the West Florida Shelf and east of the Mississippi River bird foot delta. Our study area focuses on the portion of the Mississippi Shelf spanning from near the shore near Mobile Bay to the shelf break – shown in Figure 1.1. The northern edge of the shelf is a distinct estuary environment known as the Mississippi Bight that stretches from the Gulf coastal states of Louisiana, Mississippi, and Alabama through portions of the Florida panhandle. The Mississippi Bight is bordered by multiple island chains that act as boundaries between it and nearby estuarine sounds – including the Mississippi and Alabama barrier islands and the Louisiana Chandeleur Islands. The shelf is very broad and gently sloping as it slowly deepens from the shallow nearshore to depths near 100 m at the shelf break – over 100 km from shore. The Mississippi Shelf is bordered at the shelf break where it rapidly drops in depth into the Mississippi Canyon and DeSoto Canyon.

Figure 1.1 *Northern Gulf of Mexico and Mississippi Shelf*

Location of the Mississippi Shelf, Texas-Louisiana Shelf, and West Florida Shelf within the northern Gulf of Mexico. The area of the Mississippi Shelf is shown in the black box. Our study area within the Mississippi Shelf is shown in the white box. Bathymetry data from the National Geophysical Data Center (NGDC).

1.2 Stratification and Seasonality

The temperature seasonality of the Mississippi Shelf is strongly affected by the nearby loop current. The loop current brings warmer water into the Gulf of Mexico which affects the northeastern shelf more due to its proximity. In the summer, the Mississippi Shelf water warms much earlier in the season than the Texas-Louisiana Shelf as warmer waters from the south arrive from the Loop Current. The Mississippi Shelf has an overall warmer water column and a shallower thermocline during the summer. However, during the winter months, the Mississippi Shelf waters cool slower than the Texas-Louisiana Shelf water as the loop current continues to bring warmer water from the south. A plot of vertical temperature profiles for the northwestern Mississippi Shelf can be seen in Figure 1.2.
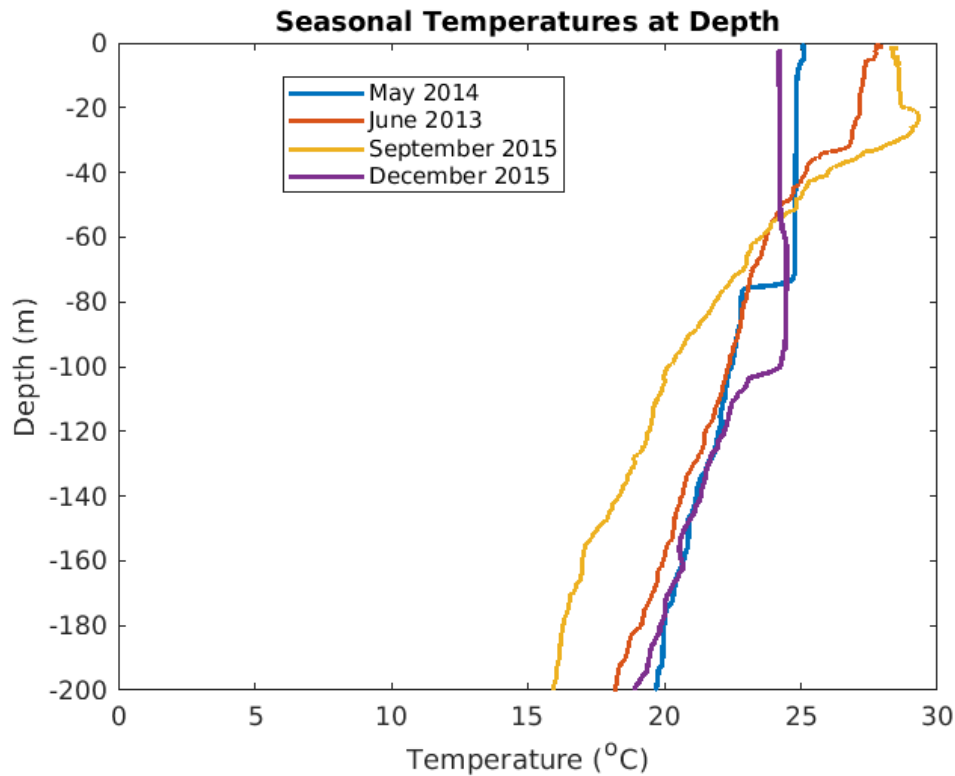
Figure 1.2 *Seasonal CTD Casts in the Northern Gulf of Mexico.*

Temperature plotted against depth from CTD casts collected in the northern Gulf of Mexico at different seasonal times. Data is from the Gulf of Mexico Research Initiative Information and Data Cooperative (data.gulfresearchinitiative.org).

The northern Gulf of Mexico receives large amounts of fresh water from a multitude of river systems – with the most notable being the Mississippi River. The influx of fresh water into the saltier Gulf causes a natural density stratification between the different water masses. This can influence the buoyancy-driven circulation and cross-shelf transport of the area (Hetland and DiMarco, 2012; Arnone et al., 2016).

The Mississippi River plume of fresh water and sediment typically drifts in a southerly or westerly direction, however, wind or eddy derived flows can routinely cause packets of fresh water from the Mississippi River plume to travel eastward as well (Walker et al., 2005). The Mississippi River plume has been shown to have a significant impact on circulation on the Louisiana-Texas shelf (Hetland and DiMarco, 2012) and the

3

Mississippi Shelf (Arnone et al, 2016). Other rivers that drain into the northern Gulf of Mexico create smaller plumes that are still important in forcing stratification along the shelf.

Since the volumes of water that flow from the Mississippi River into the Gulf of Mexico are fresh and thus lighter, the flow creates a large plume with distinct stratification between the fresh and saltwater. Throughout the Mississippi River plume, the freshwater generally forms stratified water masses above the salty Gulf water in three stages (Walker et al., 2005): 1. Fresh sediment-laden water at the surface; 2. Shallow, fresh-to-brackish turbid water below the surface; 3. Diluted Gulf of Mexico water that has become mixed with the fresh water.

1.3 Mesoscale Motions

Winds are an important driver in strong mesoscale motions on continental shelves. As wind stress is applied to the water surface, a net transport of water occurs at a 90° angle to the right of the wind in the northern hemisphere due to the Coriolis force. This transport is known as Ekman transport. In coastlines oriented along the east-west axis, upwelling events are caused by eastward alongshore wind creating offshore surface flow and onshore bottom flow, and downwelling events are caused by westward alongshore wind causing onshore surface flow and offshore bottom flow. Upwelling is an important form of mass transport and circulation as it can bring colder, nutrient-rich water to the surface allowing for more active biological productivity, and downwelling brings warmer, oxygen-rich water to lower depths, allowing for deeper biological productivity. Both upwelling and downwelling events are not bound to ocean boundaries

4

however and can occur farther offshore through Ekman pumping if wind stress curl in the horizontal wind field is available (Price et al., 1987; Knauss and Garfield, 2017).

In the northern Gulf of Mexico, the wind is an important driver of current variability (Dzwonkowski and Park, 2010; 2012) and mixing. The winds predominantly blow to the west for most of the year (Ohlmann and Niiler, 2005; Johnson, 2008) which is favorable for downwelling on the shelf. During the summer months, winds blowing to the north and northwest are dominant (Ohlmann and Niiler, 2005; Johnson, 2008) which also favors downwelling. Both wind-induced upwelling and downwelling events have been recorded on the Mississippi shelf (Dzwonkowski and Park, 2012; Coogan et al., 2019). These events are identified by changes in direction for bottom and surface velocities as well as by the movement of stratification up or down in the water column as seen in Figure 1.3.
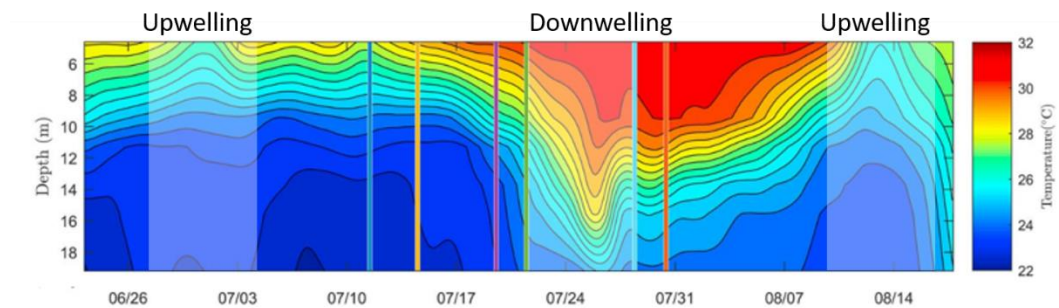
Figure 1.3 *Upwelling and Downwelling in the Northern Gulf of Mexico.*

A 2016 temperature time series plot from a mooring on the Mississippi Shelf outside of Mobile Bay. Vertical lines denote transect survey dates not discussed in this thesis. A downwelling event is seen on July 25. Two upwelling events are seen on July 6 and August 10. Modified from Coogan et al. (2019).

1.4 Surface Tides

Lunar-solar surface tidal forcing is a very important contributor to the movement of surface water throughout the global ocean. Surface tides are nondispersive kelvin

waves meaning their phase speed (C) is independent of wavelength. They propagate at a phase speed

$$C = \sqrt{gh} \tag{1}$$

where g is gravity and h is water depth. Surface tidal currents are rotary, following the path of an ellipse during one complete tidal cycle. As the tidal current approaches the shore, the major axis of the tidal ellipse changes to become parallel to the shore. Determining the major axis, minor axis, and amplitudes of tidal ellipses is further discussed in Codiga (2011). Studies have found that 11 tidal constituents are the most important in describing the lunar-solar tidal forces (Kantha, 1998; 2005). These include the semidiurnal constituents M2, S2, N2, and K2; the diurnal constituents K1, O1, P1, and Q1; and the long-period constituents of Mf, Mm, and Ssa. These constituents are further detailed in Table 1.1.

The Gulf of Mexico has relatively weak surface tides, and they have been thoroughly studied. Diurnal (K1, O1, P1, Q1) and semidiurnal (M2, S2, N2, K2) constituents make up a significant portion of the total tidal energy in the Gulf of Mexico, with long-period constituents (Mf, Mm, Ssa) not being significant. Tidal maps with the amplitude and phases of the K1 and M2 tides in the Gulf of Mexico are shown in Figure 1.4. Tidal phases progress into the Gulf from the Yucatan Channel (Seim et al., 1987; Gouillon et al., 2010) and to a much lesser extent from the shallower Florida Strait (Kantha, 2005).

Table 1.1

Tidal Constituents

Tidal Constituent	Period (Hours)	Description
M2	12.42	Principal Lunar Semidiurnal
S2	12.00	Principal Solar Semidiurnal
N2	12.66	Larger Lunar Elliptic Semidiurnal
K2	11.97	Lunisolar Semidiurnal
K1	23.93	Lunisolar Diurnal
O1	25.82	Principal Lunar Diurnal
P1	24.07	Principal Solar Diurnal
Q1	26.87	Large Lunar Elliptic
Mf	327.90	Lunar Fortnightly
Mm	661.30	Lunar Monthly
Ssa	4383.00	Solar Semiannual

The 11 major tidal constituents, their period, and a brief description of each.

Due to the natural flow of currents through the Yucatan Channel and then out the

shallow Florida Strait, the Gulf of Mexico acts as a Helmholtz resonator from the co-

oscillations of the Atlantic Ocean and the Caribbean Sea at a natural period of 1.2 days

(Seim et al., 1987; Kantha, 2005). The near-resonance of diurnal tidal periods with this

natural period of the Gulf of Mexico allows for diurnal constituents to be dominant and

nearly uniform throughout most of the Gulf of Mexico. Along the coasts of the

Mississippi shelf, the average tidal range is only 0.6 meters (Handley et al., 2012) with

the lunar diurnal O1 and K1 constituents providing the highest tidal energy (Gouillon et

al., 2010) (Figure 1.4).

Weak semidiurnal and mixed tidal cycles are found on the far eastern and western

ends of the Gulf due to semidiurnal tidal amplification across wide shelves (Kantha,

2005; Gouillon et al., 2010) as seen in Figure 1.4. This causes some areas of the West

Florida Shelf to see strong semidiurnal tides with M2 tidal currents amplified to 40 – 50

cm/s near Apalachicola Bay towards the Florida Bay and roughly 12 cm/s along the shelf break (Kantha, 2005). The largest semidiurnal tidal range occurs on the West Florida Shelf with an amplitude of 37 cm for M2 and 11 cm for S2 (Kantha, 2005). Comparatively, on the Mississippi Shelf, the M2 tidal currents vary from around 6 cm/s near shore to 1 cm/s near the shelf break (Kantha, 2005).
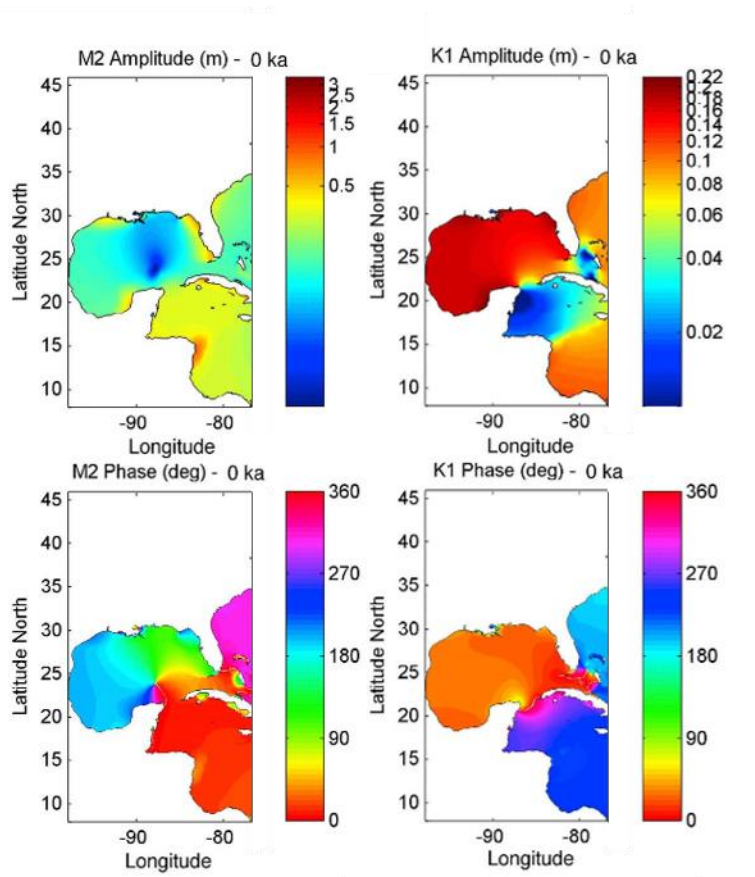
Figure 1.4 *M2 and K1 Tidal Amplitudes and Phases.*

An example of M2 and K1 tides in the Gulf of Mexico, the western Atlantic Ocean, and the Caribbean Sea from a historic tidal model. The top plots show the amplitude in meters and the bottom plots show the phase in degrees. Note the logarithmic colorbars for amplitude. Modified from Hill et al. (2011).

1.5 Near-Inertial and Tidal Internal Waves

Internal waves occur below the surface at the interfaces of differing density layers of fluid. Since the difference in density between two layers of seawater is much smaller than the difference in density between surface water and air from the atmosphere, vertical displacements in the ocean are able to become vastly larger than surface wave heights. Internal waves are categorized based on their restoring forces and on their disturbing forces.

Internal waves can exist when their frequencies are higher than the inertial frequency (f) and lower than the buoyancy frequency (N) (Gerkema and Zimmerman, 2008; Buijsman et al., 2019). Their restoring forces are buoyancy and the Coriolis force (Gerkema and Zimmerman, 2008; Buijsman et al., 2019). The buoyancy frequency is defined as

$$N = \sqrt{-\frac{g}{\rho_0}\frac{\partial \rho}{\partial z}} \tag{2}$$

where g is the gravitational acceleration, ρ is the potential density, ρ_0 is the reference density, and z is depth. Motions at the buoyancy frequency are entirely vertical. The inertial frequency is defined as

$$f = 2\Omega \sin(\varphi) \tag{3}$$

where θ is the angle between the horizontal plane and the wavenumber vector.

Near-inertial internal waves form from the geostrophic adjustment of the mixed layer as it returns to equilibrium following a disturbing force, generally wind and storm events (Gerkema and Zimmerman, 2008; Gill, 1984). These near-inertial waves are generated at or near the corresponding local Coriolis frequency (f). Near-inertial

oscillations have been identified as an important source of mixing on stratified shelves (Rippeth, 2005). Given the stratification of the northern Gulf of Mexico from freshwater input, near-inertial currents may have strong effects within the region.

Many observational and model studies have examined near-inertial motions on the Texas-Louisiana Shelf (Chen et al., 1996; Chen and Xie, 1997; DiMarco et al., 2000). These studies have found that near-inertial currents are both prevalent and strong in the northwestern Gulf of Mexico and are dominantly controlled by the wind. Within the Mississippi Shelf, however, fewer studies have been performed. Gough et al. (2016) examined near-inertial motions within the northeastern Gulf of Mexico using high-frequency radar and concluded that they were predominantly due to wind forcing. Dzwonkowski et al. (2018) noted a distinct three-layer structure in the water column and found that near-inertial oscillations on the Mississippi Bight on the Mississippi Shelf near Mobile Bay were responsible for instability in the water column that caused distinct mixing events that correlated with diurnal sea breeze/land breeze patterns. Teague et al. (2007) noted strong near-inertial motions near the shelf break following Hurricane Ivan.

Internal tides are internal waves that are generated as barotropic tides flow over topographic features on the seafloor. As the tidal flow hits bathymetric features, isotherms are pushed up and down, forming internal waves with frequencies that are mainly at the tidal frequencies (Buijsman et al., 2019). Within the Mississippi Shelf, the dominant tidal diurnal frequencies exist near f, and as such, diurnal internal tides are not likely to propagate. Internal tides occurring at semi-diurnal frequencies can propagate on the Mississippi Shelf, however, since semi-diurnal surface tides in the study area very weak, it is not likely that semi-diurnal internal tides will be very strong.

Internal waves can be affected by mesoscale motions. During downwelling events, the stratification becomes weakened as the less dense surface water is forced down. As the surface water flows downward, it creates a tilting of the isotherms. After downwelling events, the stratification of the water column can continue to be subdued as vertical mixing through convection occurs (Austin and Lentz, 2002). If the stratification of the water column is weakened or completely destroyed, near-inertial motions will be suppressed. Without stratification, internal waves will not be able to form and propagate. Coogan et al. (2019) showed a distinct downwelling event on the inner Mississippi Shelf near Mobile Bay – as shown in Figure 1.3 – that was seen to cause a strong effect on the stratification.

1.6 Research Question

Past studies of mesoscale motions and inertial waves on the Mississippi Shelf have instead focused on the impacts of these motions on biological activity or oil dispersion. Due to the economic importance of fisheries within the northern Gulf of Mexico, studies focusing on the physical oceanographic processes of the Gulf have leaned toward emphasizing their impacts on biology production, biomass transport, population distributions, or biogeochemical distribution (Johnson, 2008; Arnone et al., 2016; Dzwonkowski et al., 2017). Following the 2010 Deepwater Horizon oil spill, many studies were conducted to determine the flows in the northern Gulf of Mexico and their impact on oil dispersion (Liu et al., 2011; Dzwonkowski and Park, 2012; Bracco et al., 2019).

This study will focus on the high-frequency motions and how they are modulated by mesoscale motions across the Mississippi Shelf. By examining several stations across the Mississippi Shelf, we hope to determine what kind of motions are present in the nearshore, mid-shelf, and near shelf break environments. We will aim to answer the following research questions:

1) What are the dominant motions on the Mississippi Shelf and at what frequencies do they occur?

2) What is the spatial variability of these motions?

3) What are the vertical structures of these motions?

4) How are the high-frequency motions modulated by mesoscale motions?

CHAPTER II - METHODOLOGY

This study will use multiple datasets from mooring deployments and from long-term deployed buoys. A recently deployed Acoustic Doppler Current Profiler (ADCP) and Conductivity, Temperature, and Depth instrument (CTD) mooring dataset was used. This dataset was collected between May and August 2018. In addition, we used multiple ADCP mooring datasets that were deployed between May 2004 and November 2004. Wind data was used from long-term deployed buoy stations from the National Data Buoy Center.

2.1 Data Acquisition and Formatting

The University of Southern Mississippi (USM) deployed a trawl-resistant mooring (Figure 2.2c) on the Mississippi Shelf, south of Mobile Bay between May and August 2018 for a total of 98 days at a depth of 24 m. The location of the mooring is shown in Figure 2.1 and marked as USM. This mooring contained a SeaBird SBE 37-SMP (Serial Interface, Internal Memory, and integral Pump) CTD (Figure 2.2a) and an RD Instruments Workhorse ADCP operating at 600 kHz (Figure 2.2b and Table 2.1). The ADCP averaged sampled bursts over 10-minute intervals and the CTD sampled at 15-second intervals. Since the ADCP was upward facing, the blanking distance and the overall height of the ADCP created a segment of the water column near the bottom that was not measurable. The ADCP reported a blanking distance of 1.6 m, and the top of the ADCP was at a total height of 1.1 m above the bottom (mab). This created a total layer of 2.7 mab where no measurements were taken for the USM mooring.

An upward-looking ADCP mooring dataset collected by the Shelf Energetics and Exchange Dynamics (SEED) project (Wang et al., 2005; Teague et al., 2007;) was also

used. The SEED moorings (numbered ST1 through ST6) were deployed along the outer

continental shelf and upper slope of the Gulf of Mexico between May 2004 and

November 2004. The six SEED moorings were located on the continental shelf with

depths between 60 m and 89 m. These moorings were equipped with RD Instruments

Workhorse ADCP's that operated at 300 kHz and were located 0.5 m from the bottom

surface (Teague et al., 2007). These moored ADCPs sampled at a 15-minute interval for a

bin height of 2 m. The six shallow moorings can further be grouped based on their

depths, as stations 1 through 3 are placed upon the 60 m depth contour while stations 4

through 6 are placed between 87 and 89 m in depth. The moorings at the 60 m depth

contour were considered representative of a mid-shelf environment, while the moorings

at the 88 m depth contour were considered representative of a near shelf break

environment.
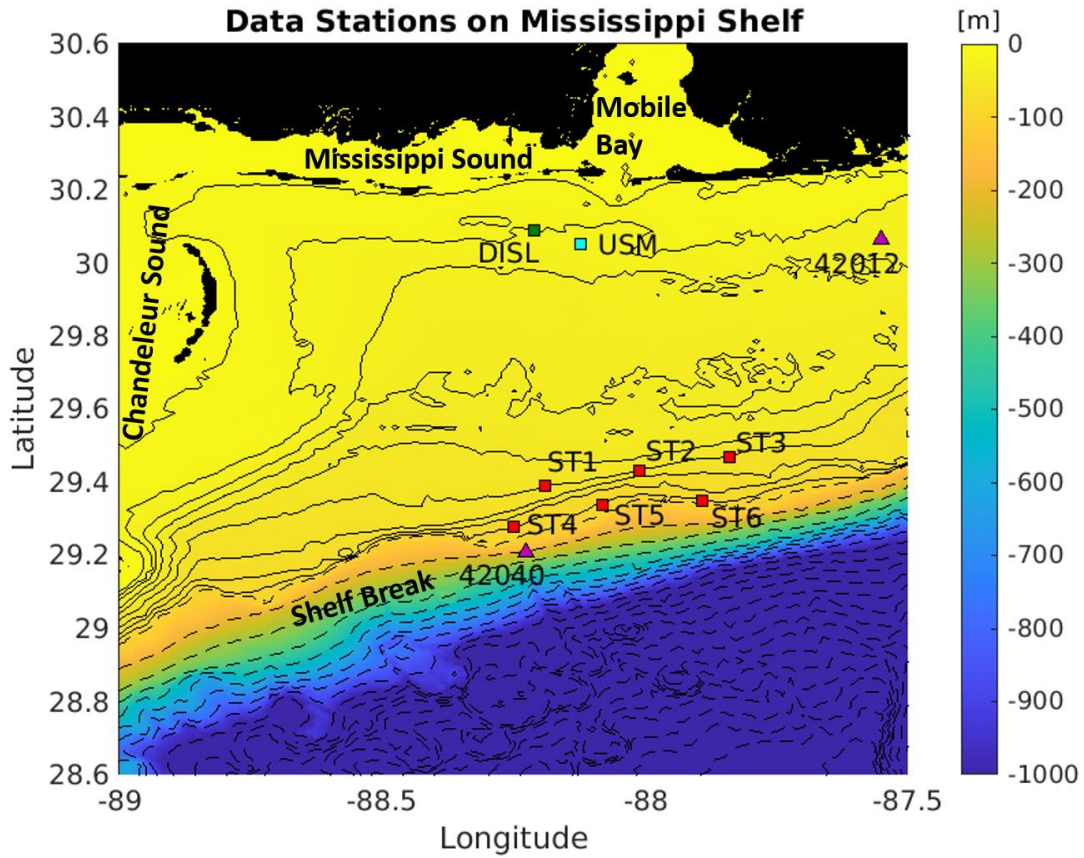
Figure 2.1 *Data Stations on the Mississippi Shelf*

A bathymetric map of the Mississippi Shelf showing the locations of the USM deployed mooring (teal square), SEED moorings (red squares), NDBC 42012 and 42040 Buoys (purple triangles), and Dauphin Island Sea Lab long term mooring (green square). Solid line contours start at 10 m depth and increase by 10 m to 90 m. Dotted contours begin again at 100 m and increase in depth by 100 m. Nearby Sounds, Mobile Bay, and the shelf break are also labeled. Note that the color axis is limited at -1000 m so as to emphasize the shelf break.

Table 2.1

Mooring Summary of ADCP Measurements.

Mooring Station	Latitude, Longitude (°)	Deployment Dates	Sampling Interval (minutes)	Top Bin Depth (m)	Bottom Bin Depth (m)	Bin Height (m)	ADCP Type
USM	30.05, -88.12	05/17/18 - 08/23/18	10	3	21	0.5	RDI Workhorse 600 kHz
ST1	29.39, -88.19	05/02/04 - 11/01/04	15	6	52	2	RDI Workhorse 300 kHz
ST2	29.43, -88.01	05/02/04 - 10/31/04	15	4	54	2	RDI Workhorse 300 kHz
ST3	29.47, -87.84	05/01/04 - 10/30/04	15	6	54	2	RDI Workhorse 300 kHz
ST4	29.28, -88.25	05/02/04 - 10/30/04	15	10	82	2	RDI Workhorse 300 kHz
ST5	29.34, -88.08	05/02/04 - 10/30/04	15	11	83	2	RDI Workhorse 300 kHz
ST6	29.35, -87.89	05/03/04 - 10/30/04	15	9	81	2	RDI Workhorse 300 kHz

Only ADCP datasets that were used in this study are shown.

Quality controlled wind and wave data were gathered from the NDBC website for

NOAA Buoy Station 42012 – Orange Beach and NOAA Buoy Station 42040 – Luke

Offshore Test Platform. Wind data at both stations were averaged over 10-minute

intervals at a height of 4 m above the sea surface. Buoy Station 42012 is located

approximately 44 nautical miles southeast of Mobile, Alabama at 30.064 N, 87.551 W.

Data was collected from Buoy Station 42012 for the months of May 2018 to August 2018

to align with the USM mooring dataset. Buoy Station 42040 is located approximately 63

nautical miles south of Dauphin Island, Alabama at 29.208 N, 88.226 W. Data was

collected from Buoy Station 42040 for the months of May 2004 to August 2004 to align

with the SEED mooring datasets.
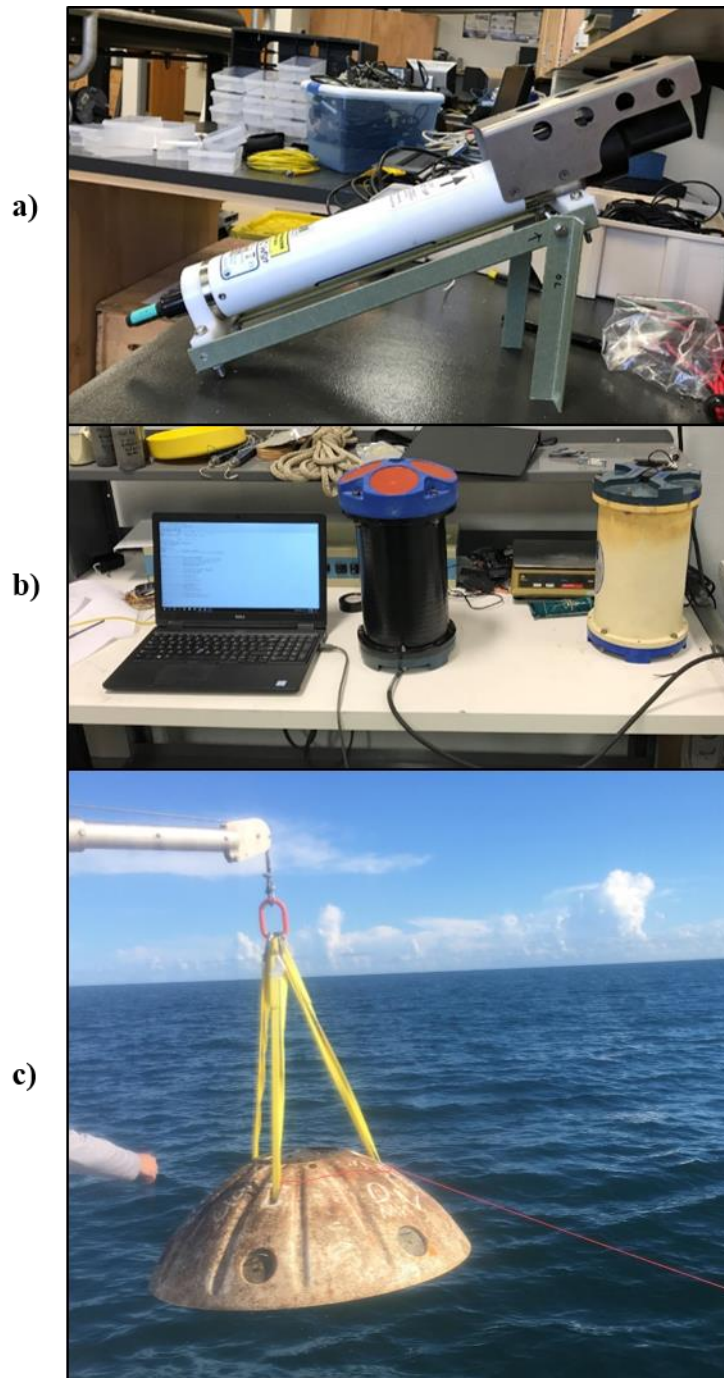
Figure 2.2 *Deployment Mooring and Instruments*

a) The Seabird SBE CTD pre-deployment. The pump intake and outtake openings are located at the top behind the protective metal

casing. b) The RD Instruments ADCP and external battery casing pre-deployment. c) The USM mooring being collected after

deployment in September 2018. The upward-looking ADCP was located exposed at the top of the mooring while the other instruments

and battery casings were enclosed within the mooring.

2.1.1 Dataset Pre-Analysis Formatting

The USM mooring data was transferred from the instruments' memory onto both external hard drives. While being collected, the data were encoded and compressed so that it could be quickly written onto the instruments' memory. The CTD data were extracted using Sea-Bird Scientific's SBE Data Processing version 7.26.7.1 program. The ADCP data were first filtered using RDI's WavesMon version 3.8 program to extract the wave data separately. The remaining ADCP data were extracted using RDI's WinADCP version 1.14 program.

2.1.2 Time Series Quality Control and Limiting

The collected datasets were then transferred into MATLAB for quality corrections and preparation for analysis. Quality control was previously done on the SEED mooring datasets, so these datasets were subsampled to the same calendar dates – though of a different year – so that they could be better compared to the USM mooring dataset. The USM mooring dataset was imported as a raw dataset, and as such, it required quality control and corrections.

The USM mooring instruments were set to record measurements until battery failure so that the longest possible time series could be recorded. Since the instruments were powered by separate battery sources, the times of the final measurements before instrument failure were not coincidental. The cut-off date of 97 days was chosen and the indices for the sample time of midnight of the 97th day were used as a time series end. This yielded a time series that spanned from May 17 to August 22, 2018.

For the USM mooring dataset, bad data bins were located and removed. Firstly, bins were identified that were registered at depths that were above the sea surface.

18

Secondly, bins near the surface were examined for incorrect and obvious data including continuous Not-A-Number (NaN) measurements and apparent anomalous measurements. Other bins were then checked for anomalous measurements and NaN values. With erroneous bins removed, the USM mooring dataset became limited to 37 bins ranging from 2.9 m below the surface to 2.7 mab (or about 21.4 m below the surface).

As previously mentioned, the SEED dataset was already quality controlled so that all available bin measurements were accurate or reliable. Since the SEED time series was much longer than the USM mooring time series, the SEED time series were limited to the same length as the USM dataset of 97-days. The reduced-length SEED dataset spanned from May 17 to August 22, 2004; so that the dates of the time series correlated with the dates of the USM mooring time series but for a different year. We also chose these dates so that the dataset does not include Hurricane Ivan, which passed over the SEED moorings on September 16, 2004 (Teague et al., 2007).

2.2 Coordinate System Rotation

For the SEED data sets, the recorded velocities were rotated such that they roughly aligned with the local bathymetry contours instead of the cardinal East and North axis. The new rotated velocities u_r and v_r were calculated by

$$u_r = u \cos(\phi) + v \sin(\phi) \tag{5}$$

$$v_r = -u \sin(\phi) + v \cos(\phi)$$

where u and v are the zonal and meridional velocities for each of the SEED stations and ϕ is the angle relative to East of the depth contour. For all SEED stations ϕ was designated as 12º. A constant angle was used for all stations because the orientation of the 60 m and 80 m isobaths lines was relatively similar. The USM mooring was not

rotated as the nearshore shelf is aligned with east. For the rest of this thesis, the r is dropped for u_r and v_r.

2.3 Separating Barotropic and Baroclinic Velocities

Barotropic velocities are depth independent velocities, and baroclinic velocities are depth dependent velocities. Through this study, the sum of the baroclinic and barotropic velocities is referred to as the "total" velocities (u,v). The barotropic motions (U,V) were calculated for all velocity datasets by averaging the velocity time series across the depth dimension. The baroclinic motions (u',v') were then calculated by removing the barotropic motions from the total velocities at each depth level such that

$$u' = u - U \qquad (6)$$

$$v' = v - V$$

The barotropic and baroclinic velocities for the USM mooring and SEED datasets were computed for the unfiltered velocity time series and for the high-passed time series.

2.4 Time Series Analysis

The collected data was transferred to MATLAB where it was analyzed by various statistical and time series analysis techniques. These techniques include bandpass filtering, empirical orthogonal function (EOF) analysis, fast Fourier transformation (FFT), rotary spectral analysis, and least-squares harmonic analysis.

2.4.1 Resolution Limiting Criterion

The effectiveness of the Fourier transformation and harmonic analyses can be determined by examining three criteria: 1. Nyquist frequency criterion, 2. Fundamental frequency criterion, and 3. Rayleigh criterion. The Nyquist frequency

$$f_n = \frac{1}{2 * \Delta t} \tag{7}$$

is the highest frequency that can be resolved, where Δt is the sampling rate (Emery and Thomson, 2004). The Fundamental frequency

$$f_0 = \frac{1}{T_0} \tag{8}$$

is the lowest frequency that can be resolved, where T_0 is the time series duration (Emery and Thomson, 2004). The Rayleigh criterion determines if two frequencies are within a minimum allowable frequency separation to be resolved separately. The Rayleigh criterion states that two adjacent frequencies (f_1 and f_2) can only be separated if

$$T_0 \geq \frac{1}{|f_2 - f_1|} \tag{9}$$

(Foreman and Henry, 1989). Tidal constituents that fall within the Nyquist and Fundamental frequencies and agree with the Rayleigh criterion can then be resolved using FFT and harmonic analysis.

We determined the minimum duration (T_0) required to resolve the M2, S2, N2, K2, K1, O1, P1, and Q1 frequencies using the Rayleigh criterion (2.2). When comparing constituents through the Rayleigh Criterion, a harmonic analysis for our time series of 97 days would not be able to differentiate between S2 and K2 and between K1 and P1. Hence, the M2, S2, N2, K1, O1, and Q1 tidal constituents were chosen for use in harmonic analysis. The Nyquist Frequency and Fundamental Frequency were also

21

calculated, and since the frequencies of the selected tidal constituents fall within the range between them, all the selected tidal constituents are discernable within the time series. The required length of time needed to resolve tidal constituents as well as the calculated Nyquist Period and Fundamental Period are shown in 2.2.

Table 2.2

Calculated Rayleigh Criterion for Paired Tidal Constituents

	T_1	0.51753	0.50000	0.52743	0.49863	0.99727	1.0758	1.0027	1.1195
T_2		M2	S2	N2	K2	K1	O1	P1	Q1
0.5175	M2		14.765	27.555	13.661	1.0758	0.99727	1.0695	0.96244
0.5000	S2	14.765		9.6137	182.62	1.0027	0.93417	0.99727	0.90354
0.5274	N2	27.555	9.6137		9.1329	1.1195	1.0347	1.1127	0.99727
0.4986	K2	13.661	182.62	9.1329		0.99727	0.92942	0.99185	0.89909
0.9973	K1	1.0758	1.0027	1.1195	0.99727		13.661	182.62	9.1329
1.0758	O1	0.99727	0.93417	1.0347	0.92942	13.661		14.765	27.555
1.0027	P1	1.0695	0.99727	1.1127	0.99185	182.62	14.765		9.6137
1.1195	Q1	0.96244	0.90354	0.99727	0.89909	9.1329	27.555	9.6137	
Nyquist Period (T_n)			0.00034722						
Fundamental Period (T_0)			97.000						

The calculated Rayleigh Criterion time series duration required for pairs of the main eight tidal constituents, the calculated periods for Nyquist Frequency and for the Fundamental Frequency are shown. All periods are shown in units of days. Cells highlighted in red show constituent pairs that cannot be separated in our harmonic analysis as they would require a longer time series duration.

2.4.2 Bandpass, Low-pass, and High-pass Filtering

Low-pass and high-pass filtering are filtering techniques in which frequencies within a determined cutoff frequency are isolated. With a low-pass filter, any frequency lower than the cutoff frequency is retained. With a high-pass filter, any frequency higher than the cutoff frequency is retained. For this study a cutoff frequency (f_c) of $f_c = \frac{1}{36\,h}$ will be used. After performing high-pass or low-pass filtering, frequencies outside of the selected filter can be easily retained by subtracting the filtered data from the unfiltered data set.

Bandpass filtering is a filter technique that isolates frequencies between a high frequency and low-frequency range by passing frequencies within the range and rejecting those outside the range. For this study, bandpass filtering between a cut off range of $\frac{1}{30\,h}$ and $\frac{1}{20\,h}$ will be applied to velocity datasets to isolate near diurnal high-frequencies and to reduce noise when plotting.

A low-pass filter was applied to the velocity time series for all ADCP datasets to isolate all velocities with frequencies lower than f_c. It should be noted that by virtue of how they are collected, the ADCP data is already somewhat low-pass filtered as the instrument saved data is averaged into 10-minute intervals. However, the low-pass filtering applied to the collected dataset will be used to isolate different frequencies. The high-frequency motions were then isolated by removing the low-pass time series from the unfiltered time series instead of applying a separate high-pass filter. Prior to the filtering, the beginning and ends of the velocity time series were zero-padded. This was done so that any spurious oscillations – also known as "ringing" – due to bandpass filtering, will be reduced. Much of the ringing was contained within the artificial cells that were removed after the bandpass filtering.

2.4.3 Fast Fourier Transformation (FFT) Analysis

A Fourier analysis is a signal demodulation algorithm that converts a dataset from a time and space domain into a frequency domain (Emery and Thomson, 2004). Fourier transformation can only determine frequencies at set integer multiples of the fundamental frequency (f_0) to the Nyquist frequency (fn) such that $F = f_0,\ 2f_0,\ 3f_0, \ldots f_n$. A fast Fourier transformation is more computationally efficient than the traditional discrete Fourier

23

transformation (Emery and Thomson, 2004). However, both produce the same results. An FFT is performed to determine which motions at what frequencies contain the most energy.

In this study, we also perform a rotary spectral analysis which involves the separation of the combined velocity vectors into rotating clockwise and counterclockwise components. For this study, a rotary spectral analysis is performed using methods described by Gonella (1972). The rotary spectra can be used to identify certain processes with known rotational directions. For example, in the northern hemisphere, inertial motions are found entirely within the clockwise spectra.

2.4.4 Harmonic Analysis

Harmonic analysis is a form of signal demodulation in which amplitudes and phases of predetermined tidal frequencies are using a least-squares fitting technique. This differs from a standard Fourier analysis in that it uses specified frequencies instead of frequencies of multiples of f_0. A harmonic analysis is performed in this study using the selected tidal frequencies mentioned in section 2.3.1 to isolate tidal motions. The harmonic analysis is performed for all depth layer times series. To obtain the best possible tidal fit using the harmonic analysis, the velocity datasets are high-passed to remove low-frequency variability.

The least-squares harmonic analysis was then performed on the high-passed velocity time series. A fit for the selected tidal constituents (M2, S2, N2, K1, O1, and Q1) to the high-passed velocity time series was then isolated so that a time series of exclusively tidal motions could also be available for analysis. Since the inertial frequency

is very close to the diurnal tidal frequency in the study area, the harmonic analysis cannot differentiate between known diurnal tidal frequencies and the inertial frequency.

2.4.5 Empirical Orthogonal Functions (EOF)

An EOF analysis creates a decomposition of the spatial and temporal variability from a time series data set in terms of orthogonal functions – or standing wave "modes" (Emery and Thomson, 2004). For this study, the EOF analysis is performed on the velocity time series with a MATLAB script using methods by Noble and Ramp (2000) and Kundu and Allen (1976). By performing the EOF analysis, we are able to isolate the dominant standing wave modes (eigenfunctions) and their variability in time.

2.5 Kinetic Energy in Different Motions

Kinetic energy (KE) was calculated for unfiltered, high-passed, and tidal time series of the undecomposed total, barotropic, and baroclinic velocities. The kinetic energy for the velocity time series at each depth level was calculated using

$$KE(Z) = \frac{1}{2} \rho_0 \left(u(z)^2 + v(z)^2 \right) \tag{10}$$

in which ρ_0 is the reference density of the water and is considered a constant of 1020 kg/m^3. Using this equation, the kinetic energy time series was calculated for the total velocities, barotropic velocities, baroclinic velocities, high-frequency velocities, barotropic high-frequency motions, baroclinic high-frequency motions, tidal motions, barotropic tidal motions, and baroclinic tidal motions. To prevent bias from the shallower USM station in comparison to the much deeper SEED measurements, the kinetic energy for each station was then depth-integrated and expressed in units of *J/m²*. We then computed the ratios between the high-frequency, tidal bands, and low-frequency kinetic energies for the total, barotropic, and baroclinic kinetic energies. We also computed the

ratios between the baroclinic and barotropic kinetic energies for the unfiltered, high-frequency, and low-frequency kinetic energies. These ratios help us to determine what motions are important on the shelf.

2.6 Wind Energetics

The wind stress and wind work were calculated using the wind velocities taken from the NOAA 42012 and 42040 stations. This analysis was performed to see if the wind data had any correlation with possible near-inertial waves. First, the wind velocities were transformed from the meteorological coordinate system that describes the direction the wind is blowing from to a Cartesian coordinate system that describes the direction the wind is blowing towards. This transformation was calculated using

$$D_C = 270^o - D_m \tag{11}$$

where D_C is the new Cartesian wind direction counterclockwise relative to east and D_m is the meteorological wind direction defined clockwise relative to true north.

The wind speed ($|\mathbf{u_a}|$) that is collected by the buoy stations is the magnitude of the u and v components of the wind vector. With the corrected wind direction and the wind speed, the u_a and v_a components of the wind speed relative to the Cartesian coordinate system are calculated using

$$u_a = |\mathbf{u_a}| \cos(D_C) \tag{12}$$
$$v_a = |\mathbf{u_a}| \sin(D_C)$$

The u_a and v_a are then rotated to the local coordinate frame using Equation 5.

The wind stress was then calculated by

$$\tau_x = \rho_{air} C_d |\mathbf{u_a}| u_a \tag{13}$$
$$\tau_y = \rho_{air} C_d |\mathbf{u_a}| v_a$$

26

where ρ_{air} is the density of the air and is considered constant at 1.2 kg/m³, C_d is the dimensionless drag coefficient which is kept at a constant value of 0.0013 (Trenberth et al., 1989; Large and Pond, 1980) and $|\mathbf{u_a}|$ is the wind velocity magnitude.

The energy work applied by the wind – also referred to as the wind work – was calculated using a modified equation from Zhai et al. (2012):

$$W_e = \boldsymbol{\tau} \cdot \boldsymbol{u_w} = \rho_{air} C_d |\boldsymbol{u_a}| (u_a u_w + v_a v_w) \tag{14}$$

where $\boldsymbol{u_w}$ is the water velocity vector at the water surface, and u_w and v_w are the x and y velocity components of $\boldsymbol{u_w}$. The surface velocity was taken as the velocity from the shallowest bin at each station.

CHAPTER III - RESULTS

The examined stations were grouped based on their depth contour and location along the Mississippi Shelf. We do not show the results from all stations and instead show selected stations from each of the depth contours. The USM mooring station is used to represent the nearshore environment, SEED station 2 is used to represent the mid-shelf environment near the 60 m depth contour, and SEED station 5 is used to represent the near shelf break environment near the 88 m depth contour.

3.1 CTD Measurements

The recorded USM mooring CTD bottom measurements for potential temperature and practical salinity are shown in Figure 3.1. Three events occurred around days 10, 50, and 80 that resulted in the bottom water becoming fresher and warmer. This is indicative of a large mixing event or downwelling of surface waters. This is similar to the downwelling event seen in Figure 2.3 at the nearby DISL mooring for a different time period.
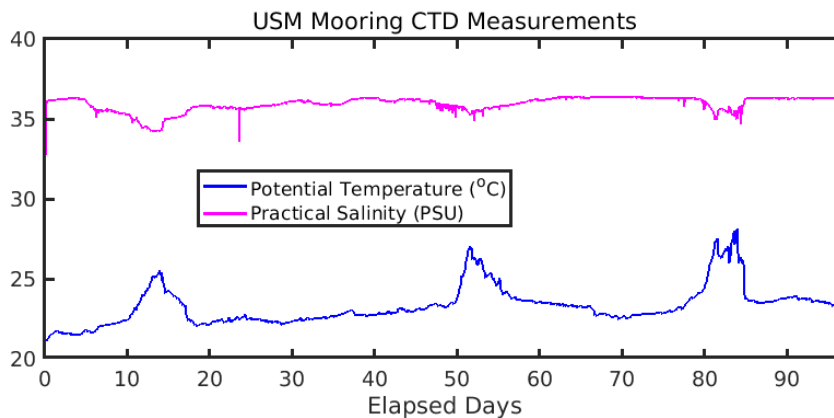
Figure 3.1 *USM Mooring CTD Measurements*

CTD bottom measurements at USM mooring at 23 m depth on the shelf. Potential temperature is shown plotted in blue, and practical salinity is shown plotted in magenta.

3.2 ADCP Measured Velocities and Bandpassed Velocities

The total unfiltered, high-passed, and low-passed along-shelf (u) velocities are plotted for the USM mooring in Figure 3.2, the mid-shelf SEED station in Figure 3.4, and the near shelf break SEED stations in Figure 3.6. For the u velocities, positive values denote eastward velocities while negative values denote westward velocities. The total unfiltered, high-passed, and low-passed cross-shelf (v) velocities are plotted for the USM mooring in Figure 3.3, the mid-shelf SEED stations in Figure 3.5, and the near shelf break SEED stations in Figure 3.7. For the v velocities, positive values denote northward velocities while negative values denote southward velocities.
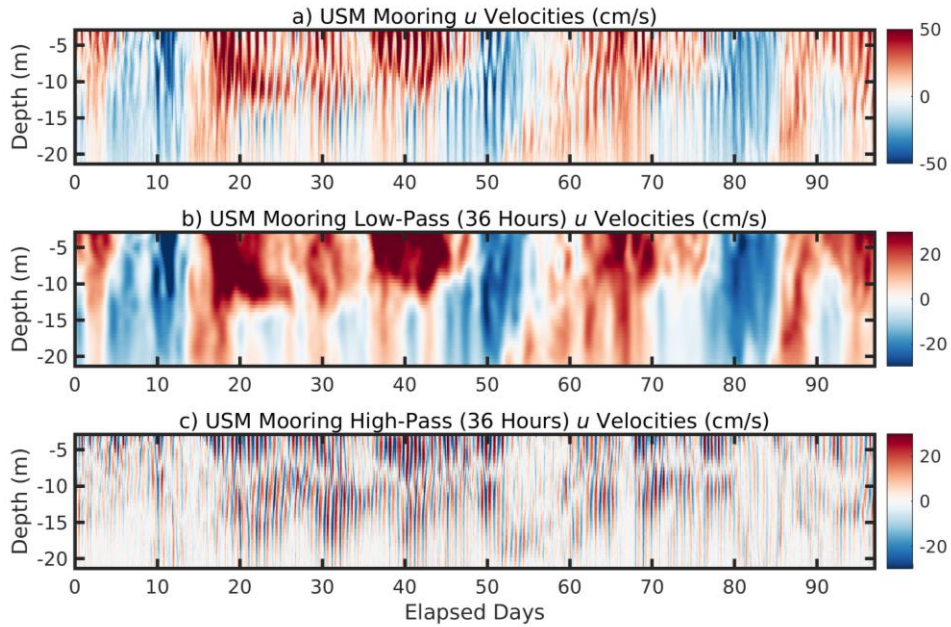
Figure 3.2 *USM Mooring u Velocities*

The total a) unfiltered, b) low-passed, and c) high-passed *u* velocities for the nearshore USM mooring. The velocities were low-passed and high-passed with a cutoff period of 36 hours. Note the change in the colorbar scale between subplots.
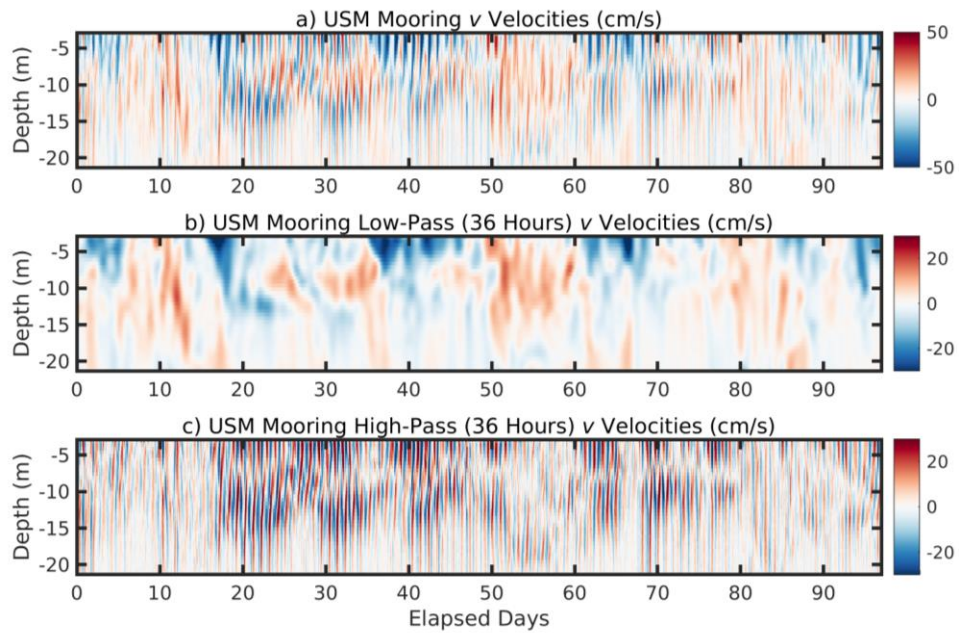
Figure 3.3 *USM Mooring v Velocities*

Same as in Figure 3.2 but for the *v* velocities.
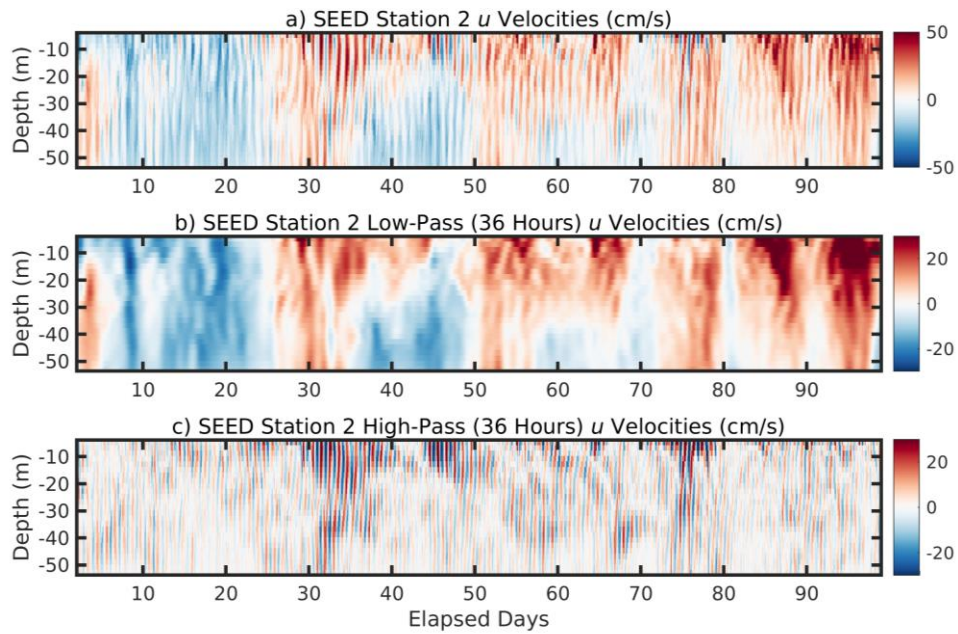
Figure 3.4 *SEED Station 2 u Velocities*

Same as Figure 3.2 but for SEED Station 2 *u* velocities.
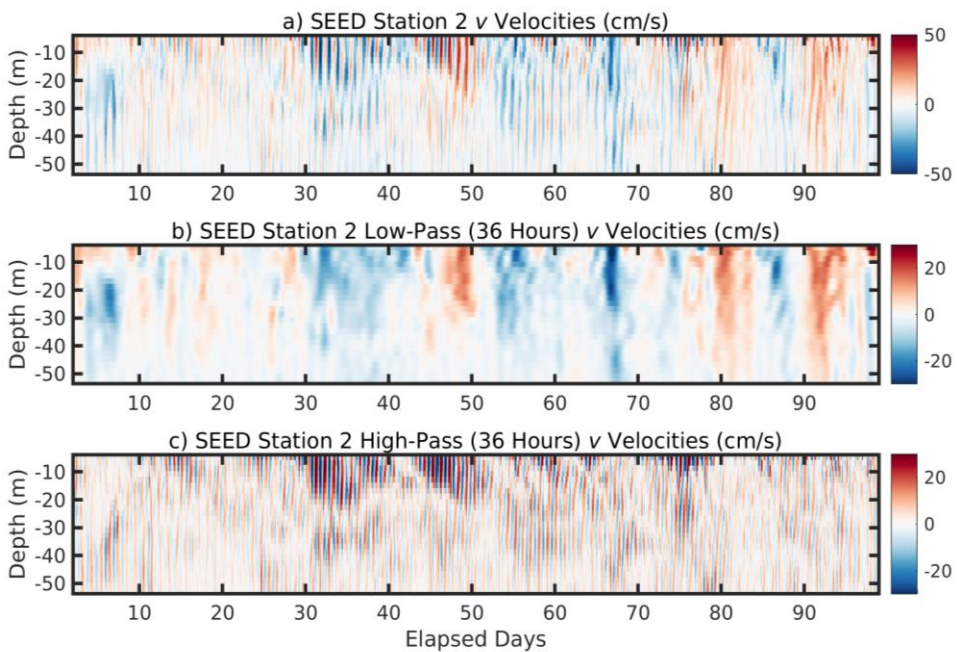
Figure 3.5 *SEED Station 2 v Velocities*

Same as Figure 3.4 but for *v velocities*.

Figure 3.6 *SEED Station 5 u Velocities*

Same as Figure 3.2 but for SEED Station 5 *u* velocities.
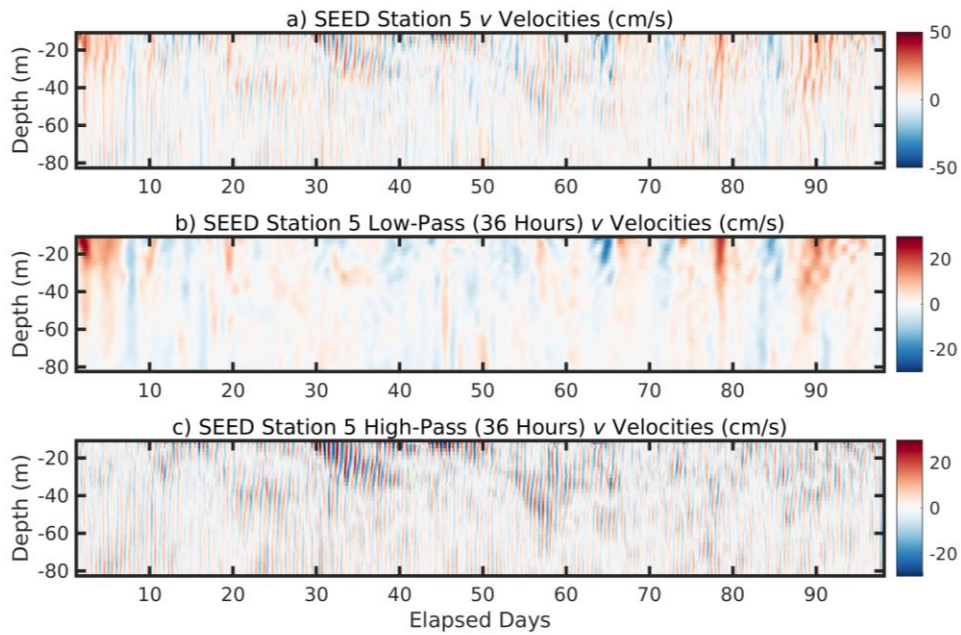
Figure 3.7 *SEED Station 5 v Velocities*

Same as Figure 3.6 but for v velocities.

Overall across the shelf, the u velocities are stronger than the v velocities. The low-frequency velocities are also consistently stronger than the high-frequency motions. The low-frequency motions appear to more consistently flow towards the east with only brief instances of westward velocities. The high-frequency motions show apparent diurnal oscillations. This is likely due to strong near-inertial oscillations.

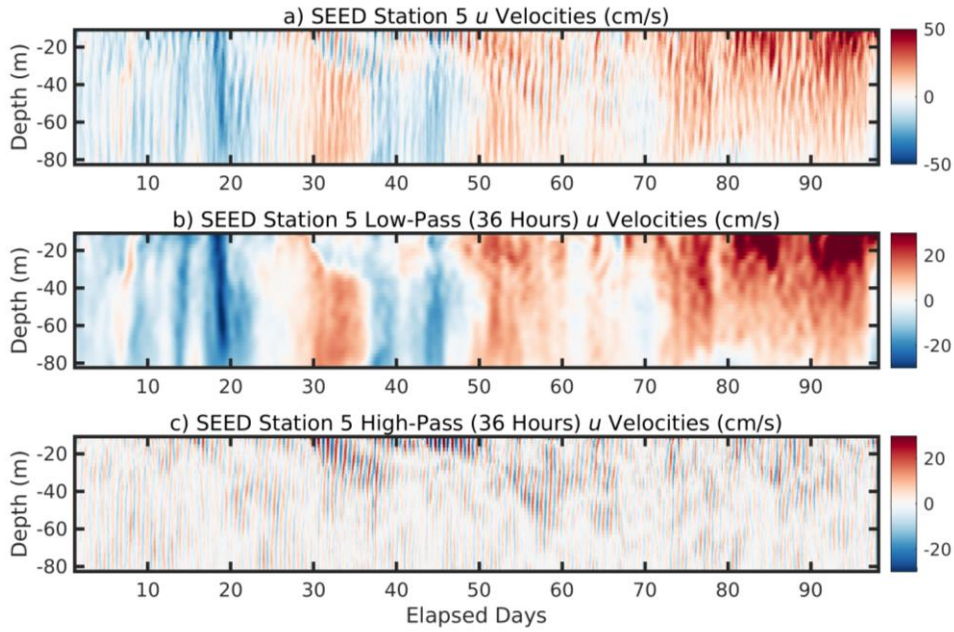The nearshore station appears to be dominated by u mesoscale (low-frequency) motions. The v mesoscale motions are much weaker than the u mesoscale motions, while the u and v high-frequency motions show similar amplitudes. Large negative (westward) low-frequency u velocities are seen in Figure 3.2b corresponding with the downwelling events seen in days 10, 50, and 80 in Figure 3.1. At these days, weak positive (northward) surface-intensified low-frequency v velocities are also seen. The high-frequency motions also appear to weaken during these days.

The mid-shelf and near shelf break SEED stations are also dominated by u mesoscale motions. Similarly to the USM station, the mesoscale v motions are weaker than the u mesoscale motions, while high-frequency motions have similar amplitudes between u and v motions. Similar strong negative low-frequency u velocity events occur at both the mid-shelf and near shelf break environments as shown in Figure 3.4b and Figure 3.6b.

3.3 Harmonic Analysis

A harmonic analysis was performed using selected tidal frequencies. The results of the harmonic analysis for the high-frequency u and v velocities for the nearshore USM station are shown in Figure 3.8 for the mid-shelf SEED station 2 in Figure 3.9 and for the near shelf break SEED station 5 in Figure 3.10. The motions at the tidal frequencies are

33

mainly diurnal and are strongest toward the nearshore and weakest at the deeper near shelf break stations. The motions appear to be similarly strong in both the u and v velocities for each location on the shelf.
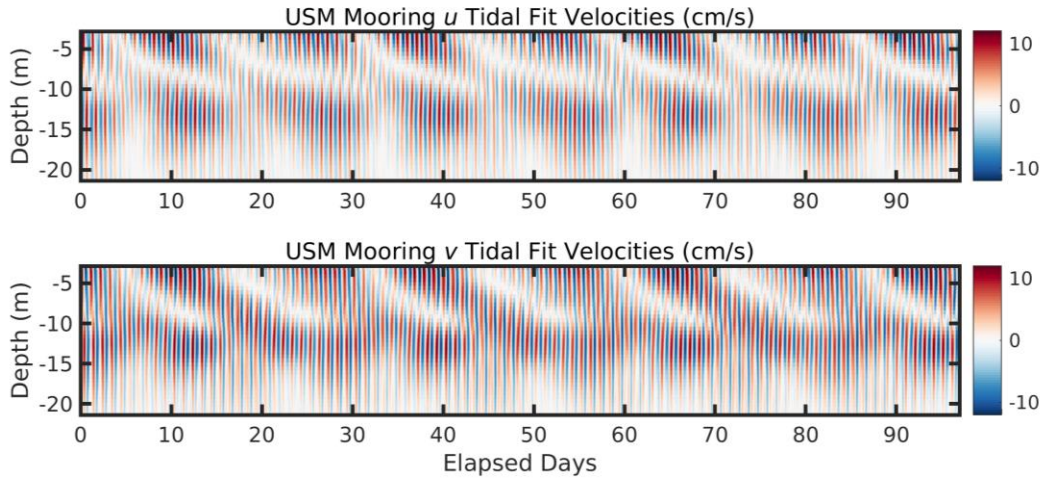
Figure 3.8 *USM Tidal Fit*

The tidal fit from the harmonic analysis performed on both the high-passed u and v velocities for the nearshore USM mooring.
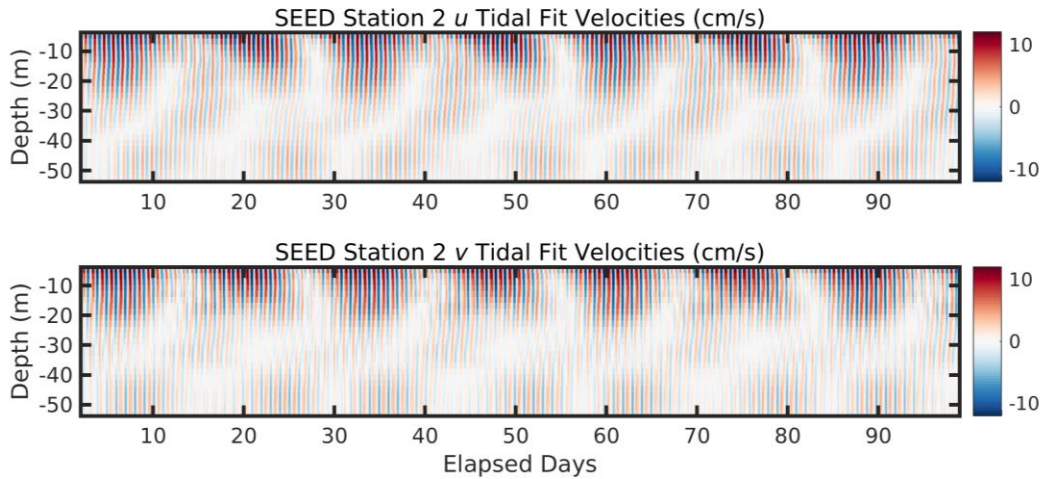
Figure 3.9 *SEED Station 2 Tidal Fit*

Same as Figure 3.8 but for SEED Station 2.
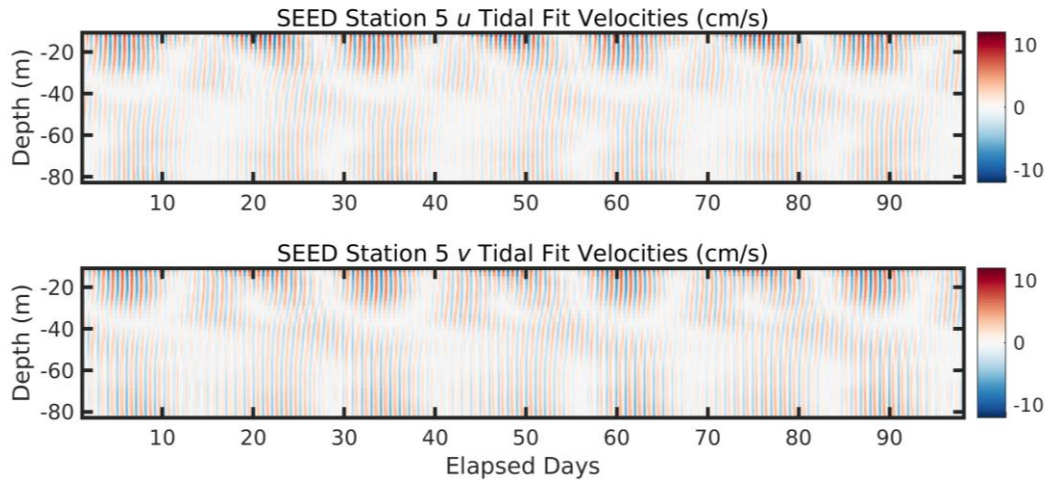
Figure 3.10 *SEED Station 5 Tidal Fit*

Same as Figure 3.8 but for SEED Station 5.

The motions fit to the tidal frequencies show an upward phase and downward energy propagation. These are indicative of internal wave motions. The energy propagating from the surface does not indicate diurnal internal tides which are instead generated from the bottom. Moreover, diurnal internal tides are also not likely because their frequencies are so close to the local f, which would not allow internal wave propagation from their possible generation at the shelf break. It is most likely that these motions are instead near-inertial waves that are propagating from the surface at the local inertial frequency. These motions are simply projected on the tidal frequencies by the tidal harmonic fit.

3.4 Kinetic Energy

Depth-integrated kinetic energy (in J/m^2) for each station was divided between the unfiltered, high-pass, and tidal energy, and also divided into the total, barotropic, and baroclinic energies. Figure 3.11 shows the time mean and depth-integrated energy of each station for the unfiltered total, barotropic, and baroclinic velocities. The depth-integrated

kinetic energy of the USM mooring, the averages of the mid-shelf stations at the depth contour of 60 m (stations 1, 2, and 3), the averages of the near shelf break stations at the depth contour of 88 m (stations 4, 5, and 6), as well as the average for all stations on the shelf are shown in Table 3.1. By examining the kinetic energy at each of the locations on the shelf, we can determine which motions are important and how their energy changes across the shelf.

Table 3.1

Average Kinetic Energy Integrated over Depth per Station

Average Kinetic Energy Integrated over Depth per Station (kJ/m^2)				
	Nearshore (23 m Contour)	Mid-shelf (60 m Contour)	Near shelf break (88 m Contour)	Overall Average
Total Kinetic Energy	52.48	72.13	103.43	76.01
Total High Pass Kinetic Energy	24.37	37.70	33.70	31.92
Total Tidal Kinetic Energy	4.30	5.88	4.68	4.95
Barotropic Kinetic Energy	21.24	29.83	62.69	37.92
High Pass Barotropic Kinetic Energy	2.39	5.40	5.56	4.44
Tidal Barotropic Kinetic Energy	1.42	2.78	2.38	2.19
Baroclinic Kinetic Energy	31.23	42.29	40.75	38.09
High Pass Baroclinic Kinetic Energy	21.98	32.30	28.15	29.89
Tidal Baroclinic Kinetic Energy	2.88	3.10	2.30	2.76

Depth-integrated kinetic energy values for the USM mooring and SEED stations, and overall averages for unfiltered, high-pass, and tidal energies based on total, barotropic, and baroclinic velocities.

As shown in Table 3.1 and Figure 3.11, a general decrease of total kinetic energy is found as the shelf depth decreases towards the shore with the total kinetic energy being greatest at the deeper SEED stations and lowest at the shallower USM station. The total energy change does not correlate exactly with the decrease in depth, as the change in total

energy between the deepest stations at the 88 m contour and the 60 m contour – a 35.66%

difference over 22 m - is larger than the change between the 60 m contour and 24 m

contour – a 31.54% difference over 36 m. No correlation between decreasing depth and

kinetic energy change can be found for the total high-frequency kinetic energy and tidal

kinetic energies. In both cases the total kinetic energy increases between 88 m and 60 m –

and increase of 11.24% in high-frequency kinetic energy and an increase of 22.73% in

tidal high-frequency kinetic energy. The total high-frequency kinetic energy and tidal

kinetic energy then decrease in depth up the shelf from 60 m to 23 m by 42.95% and

31.04% respectively.
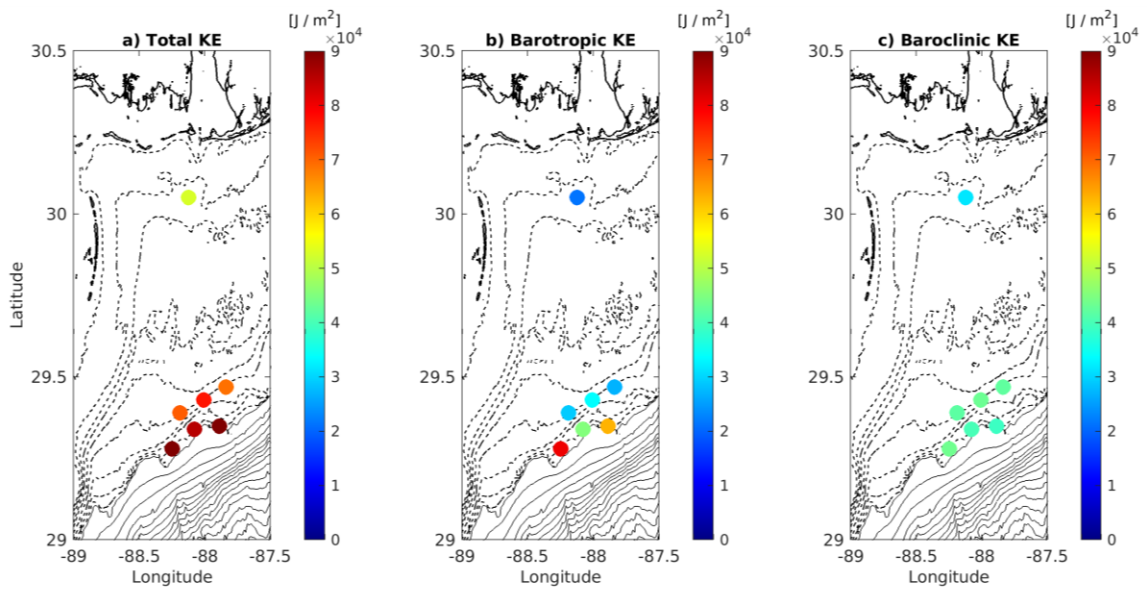
Figure 3.11 *Kinetic Energy Across the Mississippi Shelf*

Values for all stations across the shelf showing the time-averaged and depth-integrated kinetic energy for the unfiltered a) total, b) barotropic, and c) baroclinic velocities.

The largest energy differences across the shelf occur in the barotropic motions as

seen in Figure 3.11b and Table 3.1. The highest energy change is for the unfiltered

barotropic motions between the 88 m and 60 m isobaths (SEED stations) with a 71.03%

decrease and followed by a decrease of 33.64% from the 60 m isobath to the USM

mooring at the 23 m isobath. The high passed barotropic kinetic energy is much more

consistent between the SEED stations with only a small decrease in energy (Table 3.1).

However, the high passed barotropic kinetic energy then drops 77.28% from the mid-

shelf to the nearshore station – the highest percentage difference found in Table 3.1. In

contrast, the barotropic tidal motions are found to increase between the near shelf break

and mid-shelf stations and then decrease by 64.76% to the nearshore environment.

The change in energy is also not consistent between the barotropic and baroclinic

kinetic energies. While the barotropic motions generally decrease across the shelf, the

average kinetic energies are found to be highest at the mid-shelf stations for baroclinic

motions. The unfiltered baroclinic kinetic energy increases from the near shelf break to

the mid-shelf stations and then decreases by 30.09% from the mid-shelf to the nearshore

stations. The high-pass baroclinic kinetic energy increases by 13.73% from near the shelf

break to the mid-shelf where it then decreases by 38.03% to the 23 m station. The

baroclinic tidal kinetic energy increases from the near shelf break stations to the mid-

shelf stations by 29.63% and then decreases by 7.36% to the nearshore station. All

subdivided baroclinic energies increase from 88 m to 60 m and decrease from 60 m to 23

m.
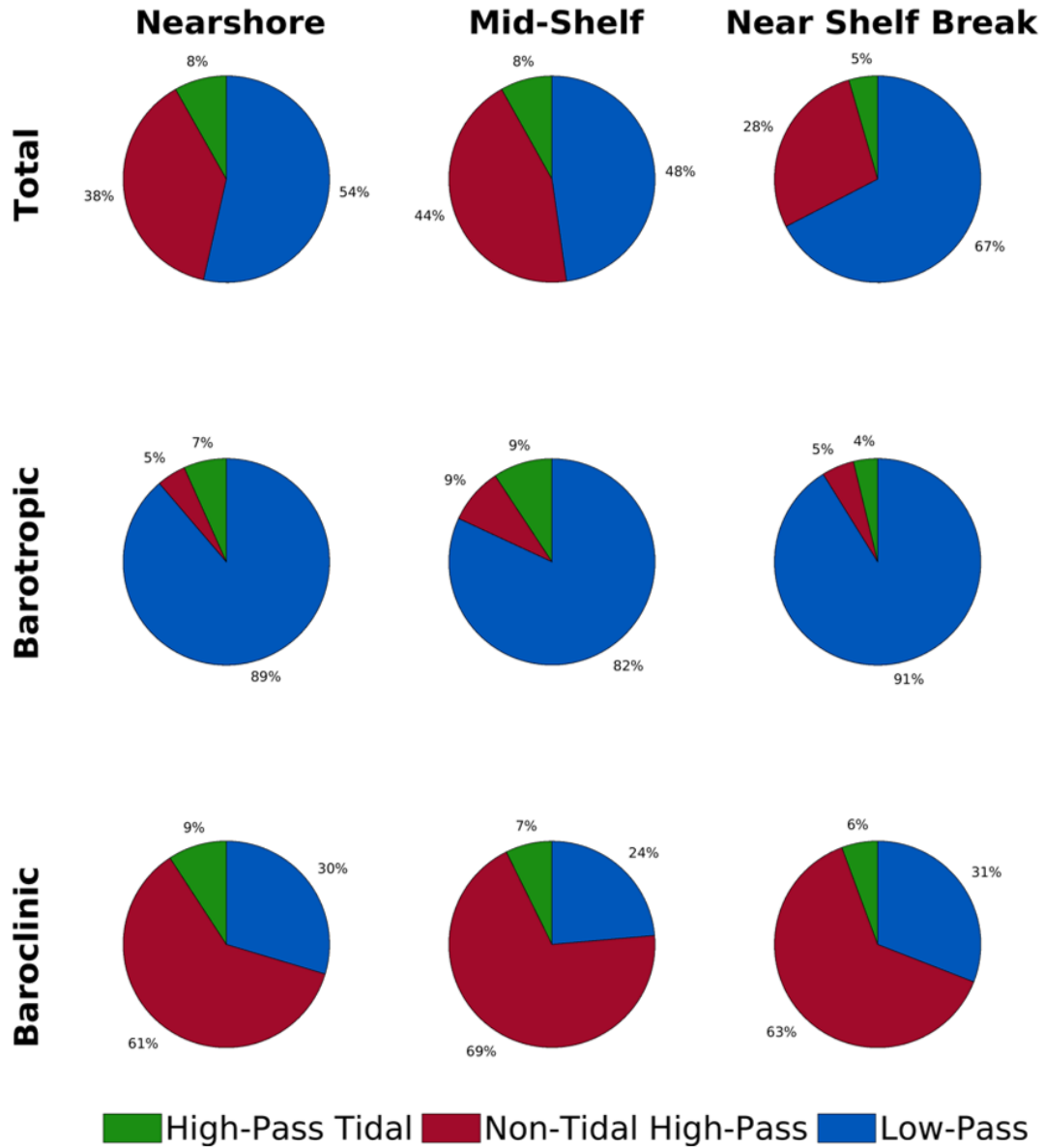
Figure 3.12 *Total, Barotropic, and Baroclinic Kinetic Energy Pie Charts*

Pie charts of depth-averaged and time-averaged kinetic energy for the USM mooring at 23 m and the averages for each of the two

rows of SEED moorings on the 88 and 60 m isobaths on the Mississippi Shelf. The kinetic energy is split into the total kinetic energy

(row 1), the barotropic kinetic energy (row 2), and the baroclinic kinetic energy (row 3). Each pie chart is split between (green) tidal

frequency kinetic energy, (red) non-tidal high-frequency kinetic energy, and (blue) low-frequency energy.

Figure 3.12 shows the tidal, non-tidal high-pass, and low-pass kinetic energy as a fraction of the total, barotropic, and baroclinic kinetic energy for the three examined depths on the shelf. This allows us to determine what types of baroclinic and barotropic motions are dominant. The breakup of the total kinetic energy (row 1 of Figure 3.12) finds that the nearshore USM station and mid-shelf SEED stations have similar ratios of energy between high and low-frequency motions. However, the near shelf break SEED stations show a different ratio between high and low-frequency motions. At the deepest stations near the shelf break, low-frequency motions make up a much higher percentage of the total variance compared to the shallower stations. Due to this large skew from low-frequency motions, the 88 m station composition contrasts the similarly structured compositions at 60 m and 23 m. This can also be seen in the unfiltered, low-frequency, and high-frequency velocities in Figure 3.2, Figure 3.4, and Figure 3.6.

Within only the barotropic motions for all three sections of the shelf (row 2 of Figure 3.12), it is obvious that low-frequency motions are most dominant. As such, barotropic high-frequency tidal and non-tidal kinetic energies were found to make up less than 18% of the total barotropic kinetic energy. While not drastically different from the other stations, the mid-shelf environment stands out within the barotropic kinetic energy composition due to the higher high-frequency kinetic energy.

In contrast to the dominant low-frequency energies in the barotropic composition, the baroclinic kinetic energy across the shelf (row 3 of Figure 3.12) appears to be dominated by high-frequency kinetic energy. Roughly 70% of the baroclinic motions are described by high-frequency motions. About 10% of the baroclinic motions appear to be due to tidal motions. However, since diurnal tides occur near local f and because semi-

40

diurnal tides are very weak, it is likely that these baroclinic motions at tidal frequencies are not tidal motions. We hypothesize that it is likely that these motions are near-inertial motions that project onto the tidal frequencies.

When examining the overall composition between high and low-frequency energies across the shelf, it is evident that there is some change that happens between the shelf break and the mid-shelf and between the mid-shelf and the nearshore. The 60 m depth stations consistently had the highest fraction of high-frequency motions. The deeper 88 m stations and the shallowest 23 m station had a higher fraction of low-frequency kinetic energy, which was noticeably pronounced in the barotropic motions.
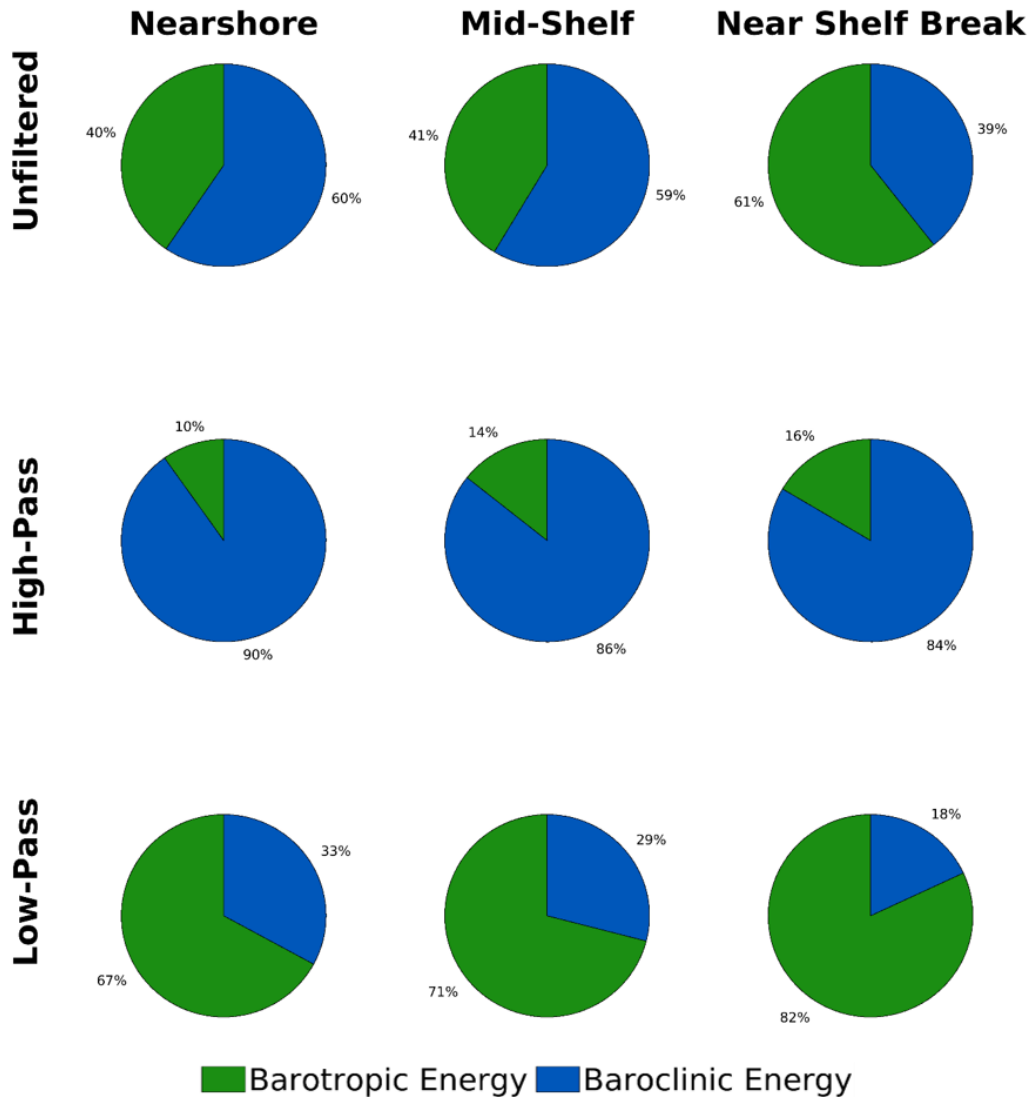
Figure 3.13 *Unfiltered, High-pass, and Low-pass Kinetic Energy Pie Charts*

Pie charts of the ratio between barotropic and baroclinic energies that comprise the unfiltered, high-passed, and low-passed kinetic energies for the USM mooring at 23 m depth, the SEED stations at 60 m depth, and the SEED stations near 88 m depth

Figure 3.13 shows the fraction of the barotropic and baroclinic energies at each of the examined depths across the shelf. By examining the breakup between barotropic and baroclinic motions, the variability across the shelf can be examined.

For the unfiltered kinetic energy, the 23 m and 60 m stations show very similar compositions between barotropic and baroclinic energies with baroclinic energies being

dominant with 60% and 59%. However, the deeper 88 m SEED stations instead show that near the shelf break, barotropic energies are dominant, making up 61% of the unfiltered kinetic energy.

The high-frequency kinetic energy is shown to be mostly baroclinic across the shelf. All stations show similar ratios in the high-frequency kinetic energy. The fraction of high-frequency baroclinic kinetic energy only slightly increases from 84% at 88 m to 90% at 23 m.

The low-frequency kinetic energy is shown to be mainly barotropic across the shelf. The 23 m and 60 m stations have similar ratios with barotropic motions making up 71% of the low-frequency motions at 60 m and 67% at 23 m. The 88 m station, however, shows a higher ratio with 82% of the low-frequency kinetic energy being explained by barotropic motions.

3.5 Rotary Spectra

A rotary spectral analysis was performed on the baroclinic velocities at all depth layers of the stations across the Mississippi Shelf to determine at which frequencies motions occur. This analysis was performed on baroclinic velocities to remove any bias in energy peaks due to barotropic tidal motions. The results of the rotary spectra can be seen in Figure 3.14, Figure 3.16, and Figure 3.17. Within the rotary spectra for all stations, the clockwise energy is dominant over the counterclockwise energy. The strongest energy signals occur over a broad spectrum near the clockwise diurnal period for all stations. This diurnal energy is most likely due to inertial motions because diurnal internal tides cannot propagate from the shelf break where they would be generated. The broadband characteristic of the energy peaks also suggests that the energy is occurring at

irregular frequencies as opposed to the tidal frequencies. A surface intensification can also be seen in the energy peaks, which is likely due to the wind forcing of the near-inertial motions. The lack of a broadband diurnal peak within the counterclockwise motions also indicates that these are near-inertial motions that rotate anti-cyclonically. Energy near the semi-diurnal period is present at all stations but is much weaker in spectral density compared to the energy near the diurnal period.
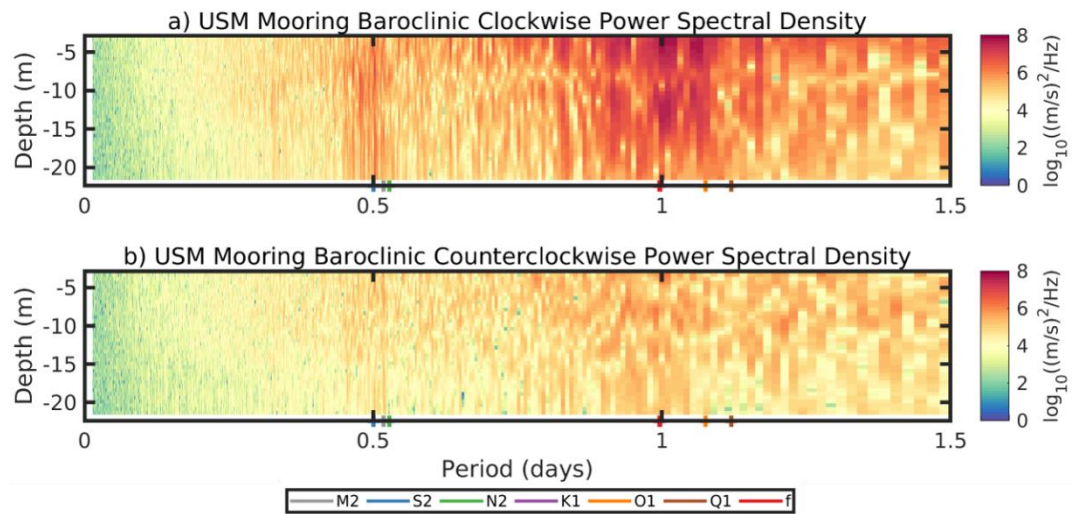
Figure 3.14 *USM Mooring Rotary Spectra*

The rotary spectra Fast Fourier Transformation for the clockwise and counterclockwise baroclinic motions at the nearshore USM station. The tidal and inertial periods are marked on the bottom of each plot with a cross. Note that at the USM station, the inertial period and K1 period overlap.

Figure 3.15 *SEED Station 2 Rotary Spectra*

Same as Figure 3.14 but for SEED Station 2.
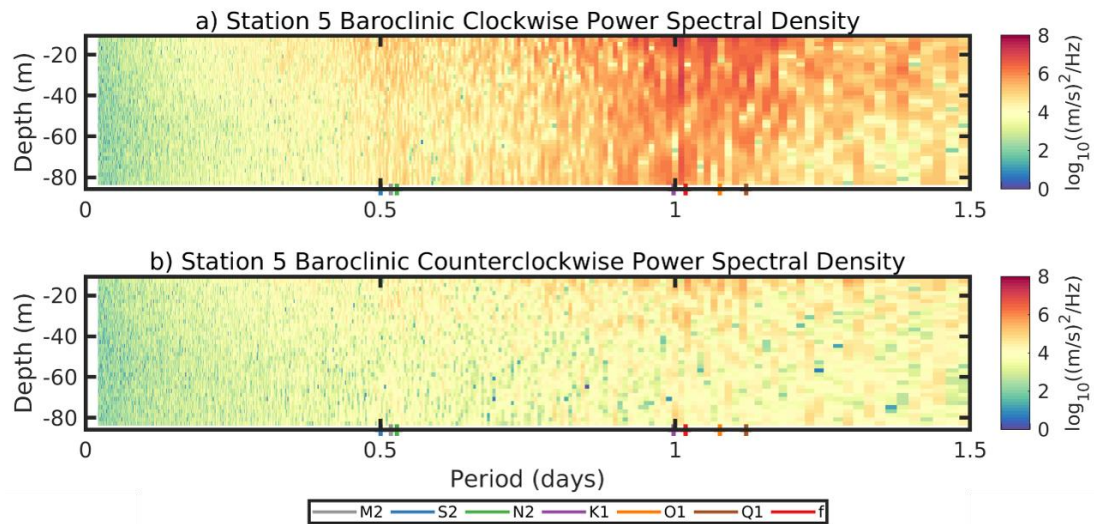
Figure 3.16 *SEED Station 5 Rotary Spectra*

Same as Figure 3.14 but for SEED Station 5.

Since the clockwise rotating motions are dominant in this area, the clockwise rotary energy is depth-averaged to more closely examine the peaks of energy. A periodogram with the energy plotted against period is shown for the nearshore USM station in Figure 3.17, for the mid-shelf SEED station 2 in Figure 3.18, and for the near shelf break SEED station 5 in Figure 3.19.
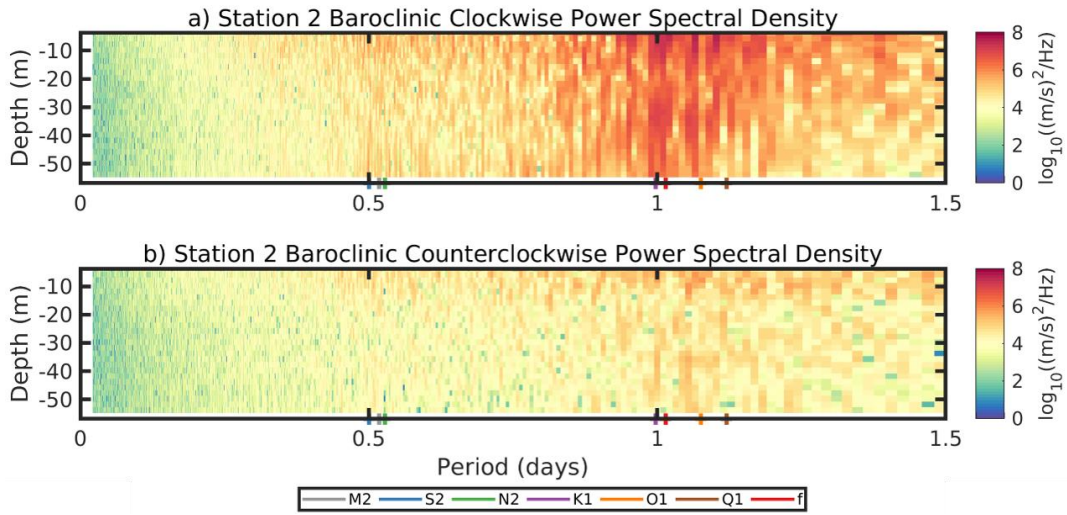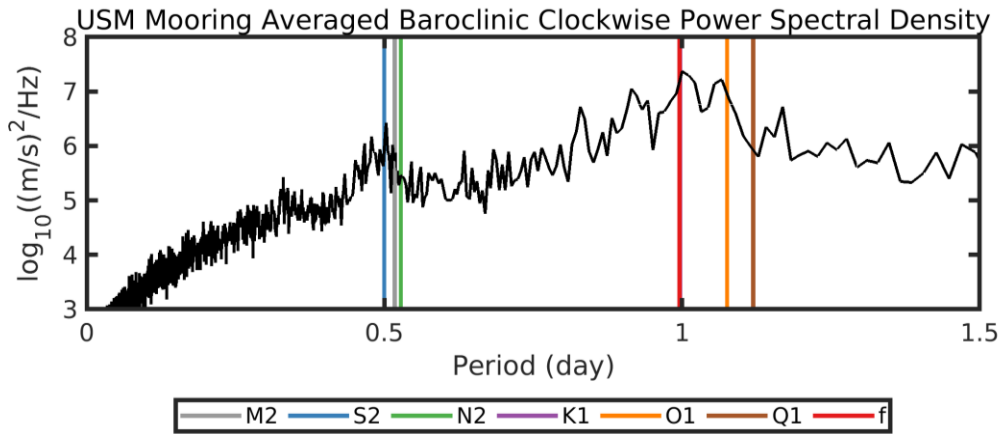

Figure 3.17 *USM Mooring Averaged Baroclinic Clockwise Rotary Spectra*

The depth-averaged baroclinic clockwise rotary spectra for the nearshore USM station. The tidal constituents and inertial periods are indicated with colored lines. Note that the periods of K1 and f overlap at this station
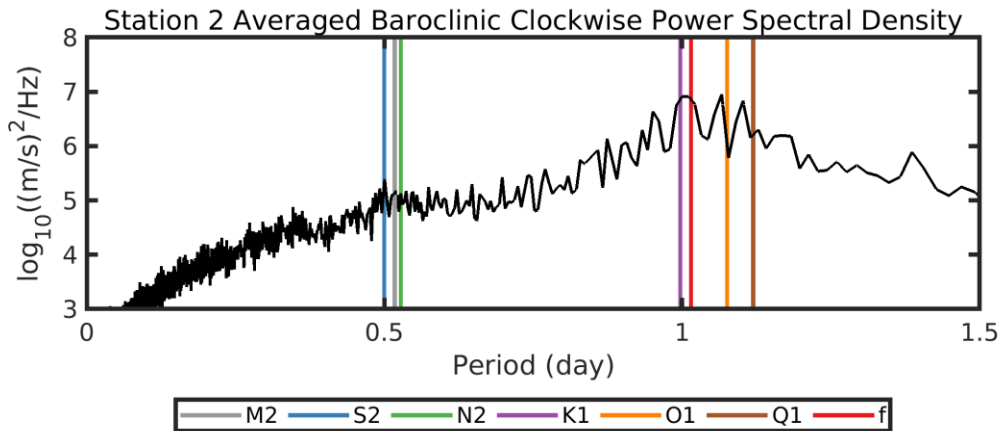
Figure 3.18 *SEED Station 2 Averaged Baroclinic Clockwise Rotary Spectra*

Same as Figure 3.17 but for SEED Station 2. Note that K1 and f do not overlap at this station.
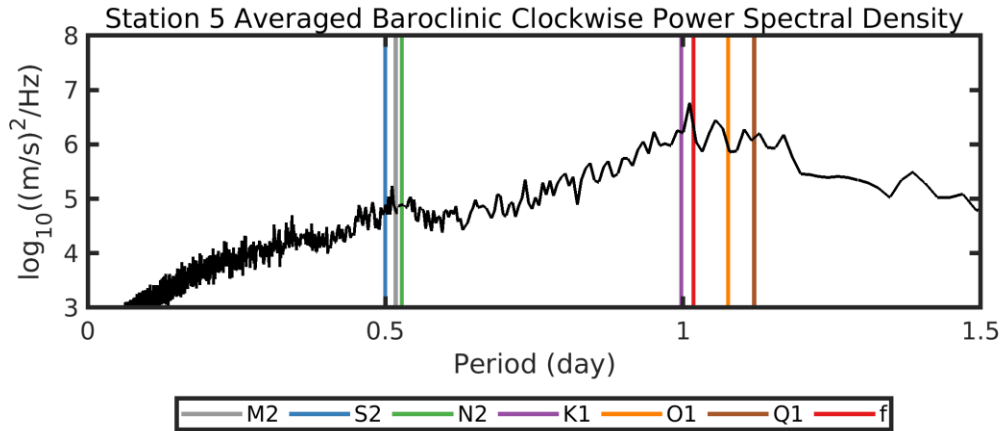
Figure 3.19 *SEED Station 5 Averaged Baroclinic Clockwise Rotary Spectra*

Same as Figure 3.17 but for SEED Station 5. Note that K1 and f do not overlap at this station.

For all stations examined, peaks in energy are seen near the tidal constituent

frequencies but they are significantly higher near the diurnal frequencies than near the

semidiurnal frequencies. Peaks near f are seen in all stations, however, it is difficult to

distinguish energy between the broader f peak and the diurnal tidal peaks, specifically

K1. At the USM station, the K1 and f frequencies completely overlap. We argue that the

broadband energy peak near the diurnal frequency is due to inertial motions that are

episodic in nature and phase shifted in time. This is further explained in Appendix A.

3.6 EOF Modes

An EOF analysis was performed to decompose the high-frequency and low-

frequency motions into several modes and into their time variability. The results of the

EOF analysis produced similar modes for each isobath group of stations. The first three

spatial EOF modes of the nearshore USM station for the high-pass u and v velocities are

shown in Figure 3.20 and for the low-pass u and v velocities in Figure 3.21. The first

three spatial EOF modes of the mid-shelf SEED station for the high-pass u and v

47

velocities are shown in Figure 3.22 and for the low-pass u and v velocities in Figure 3.23.

The first three spatial EOF modes of the near shelf break SEED station for the high-pass

u and v velocities are shown in Figure 3.24 and for the low-pass u and v velocities in

Figure 3.25. Since the spatial EOF modes were similar for each isobath, the results at

SEED stations 2 and 5 were selected.
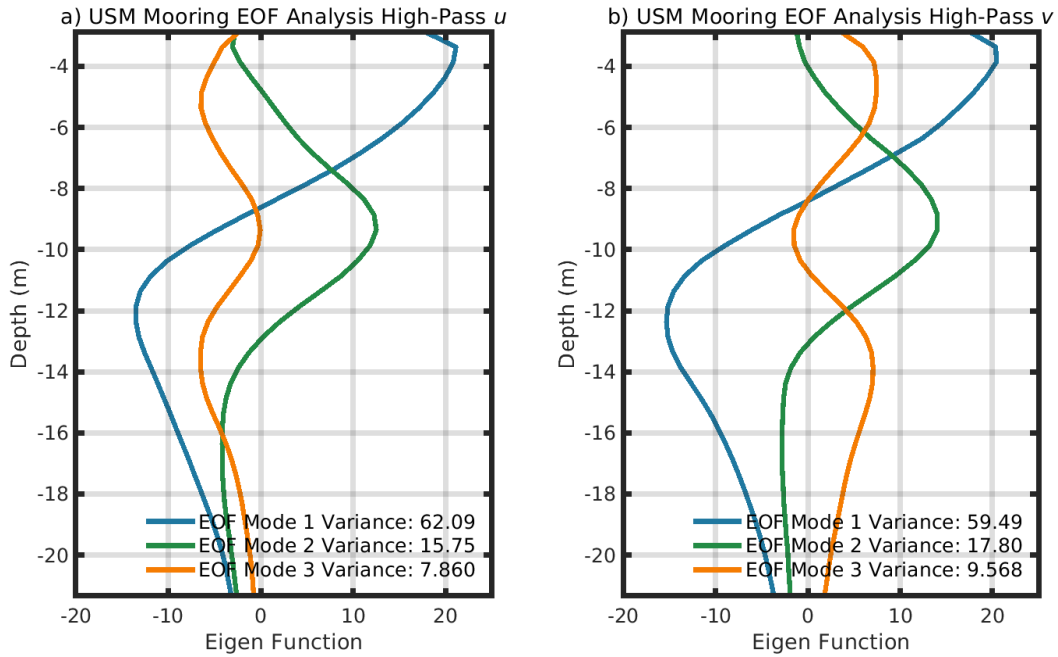
Figure 3.20 *USM Mooring High-Frequency EOF Modes*

The eigenfunctions for the first three spatial EOF modes for the high-pass *u* and *v* time series at the USM mooring located at a depth of 23 m. The fraction of the total variance for each mode is shown in the legend.
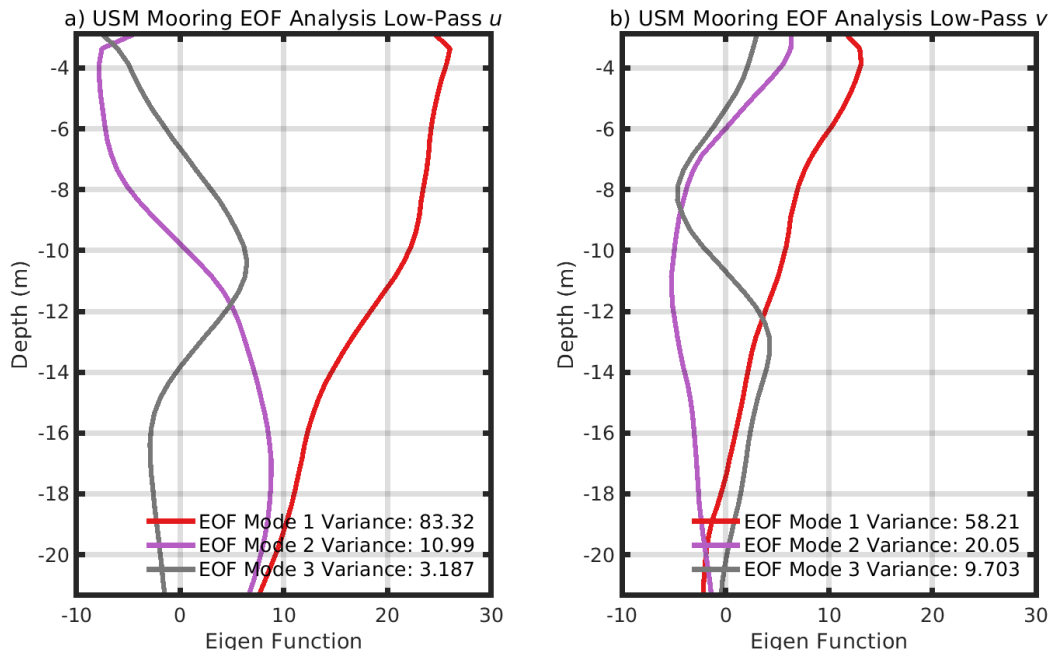
Figure 3.21 *USM Mooring Low-Frequency EOF Modes*

Same as in Figure 3.20 but with low-pass *u* and *v* modes.
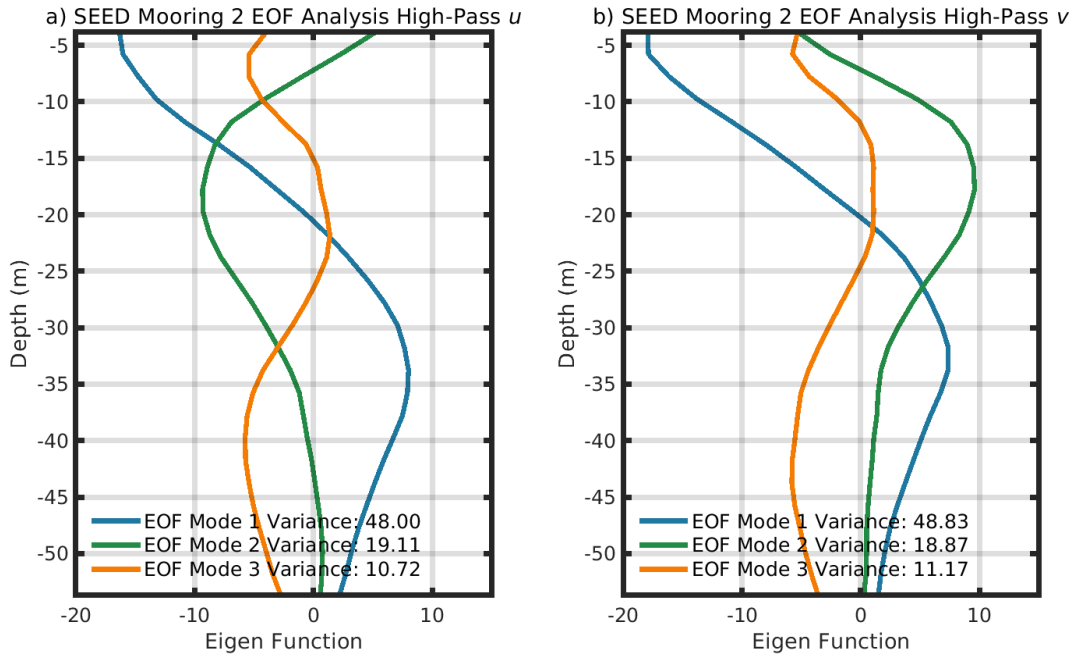
Figure 3.22 *SEED Station 2 High-Frequency EOF Modes*

Same as Figure 3.20 but for SEED Station 2.
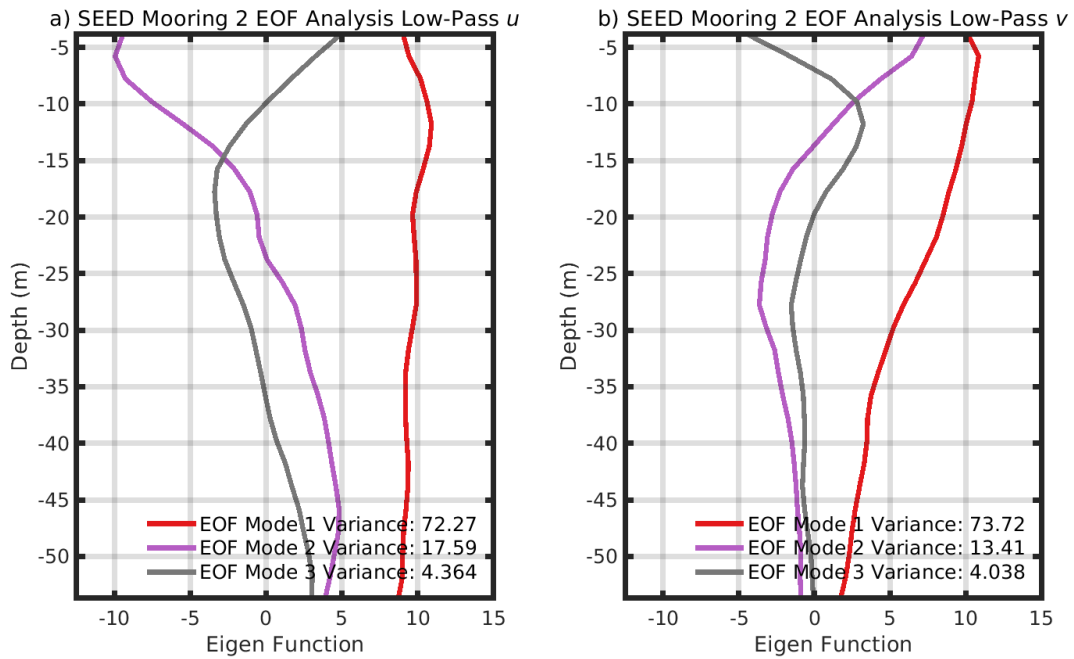
Figure 3.23 *SEED Station 2 Low-Frequency EOF Modes*

Same as Figure 3.21 but for SEED Station 2.
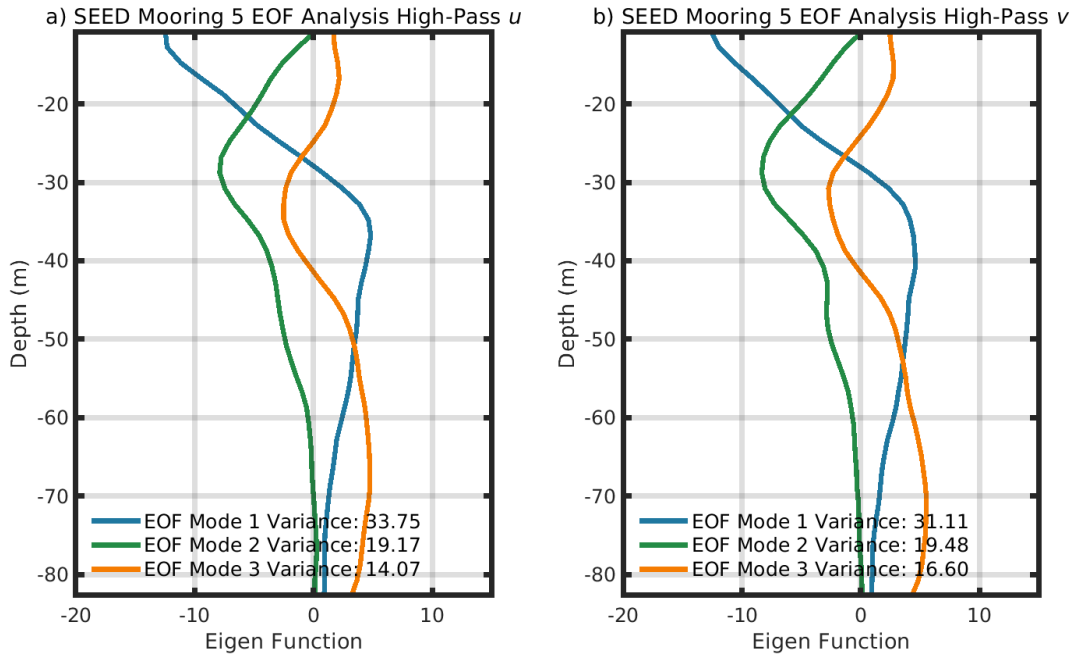
Figure 3.24 *SEED Station 5 High-Frequency EOF Modes*

Same as Figure 3.20 but for SEED Station 5.

Figure 3.25 *SEED Station 5 Low-Frequency EOF Modes*

Same as Figure 3.21 but for SEED Station 5.

The high-pass EOF modes for all stations across the shelf are similar. Each station shows a very strong mode 1 in both u and v velocities. The high-pass mode 1 motions at all stations are dominated by out of phase motions, i.e. the bottom velocities are 180º out of phase with the surface velocities. Across the shelf, the high-pass u and v modes are very similar at each station. This is indicative of near-inertial motions that occur everywhere across the shelf. The stations do show some d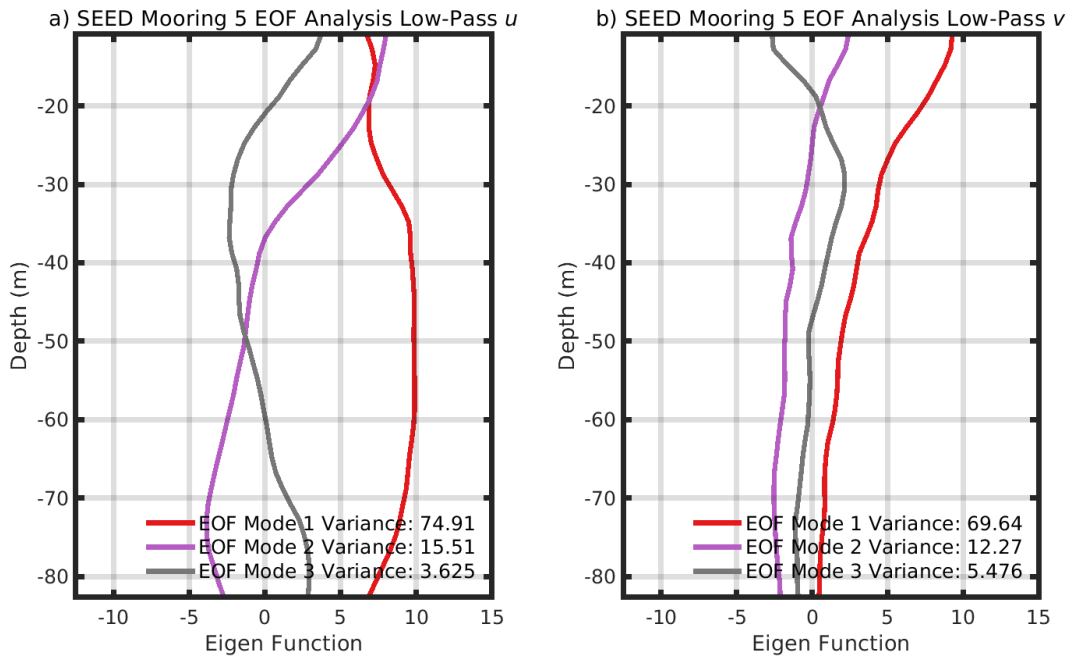ifferences in the total variability of the modes with the dominant mode 1 making up less of the total variability in the deeper stations.

Within the low-frequency EOF modes, the stations show more differences. At the nearshore USM station, a strong mode 1 with vertical shear is seen in the alongshore u velocities. This is paired with a strong mode 1 with out of phase motions for the low-pass cross-shore v velocities. This can be associated with downwelling and upwelling processes, which we will discuss in the Discussion and Conclusions section. At the mid-shelf and near shelf break stations, the mode 1 u eigenfunctions are very barotropic, while the mode 1 v eigenfunctions lack the out of phase surface and bottom motions that are seen at the USM station. This suggests that the upwelling and downwelling processes are likely not present closer to the shelf break.

Figure 3.26 shows the temporal components of the EOF mode 1 for the low-pass u and v plotted against the temporal components of the mode 1 high-pass u and v. This shows that the high-pass motions are clearly dominated by diurnal frequencies which would again indicate near-inertial motions. The high-frequency motions are shown to change in strength at different times. Within the low-pass EOF modes, it appears that the change in direction of the low-pass u velocities may affect the strength of the high-

52

frequency EOF modes. This is generally seen during periods when the low-frequency *u* mode 1 component is negative (westward) which is indicative of downwelling. Figure 3.27 shows the low-passed and high-passed mode 1 time series for the *u* velocities at all stations. At the mid-shelf and near shelf break stations, a negative low-pass mode 1 *u* does not correlate as well with weaker high-pass mode 1 *u*, which further suggests that downwelling processes do not have as strong of an effect as seen in the nearshore station.
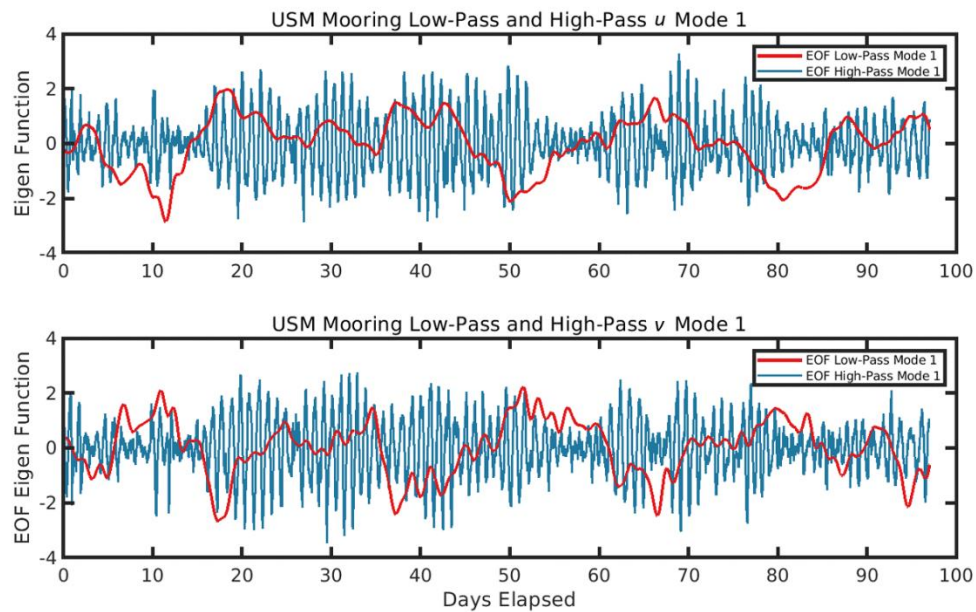
Figure 3.26 *USM Mooring Mode 1 Low-pass and High-pass u and v Time Components*

The time component of mode 1 low-pass (red) and the mode 1 high-pass (blue) u and v velocities at the USM station.
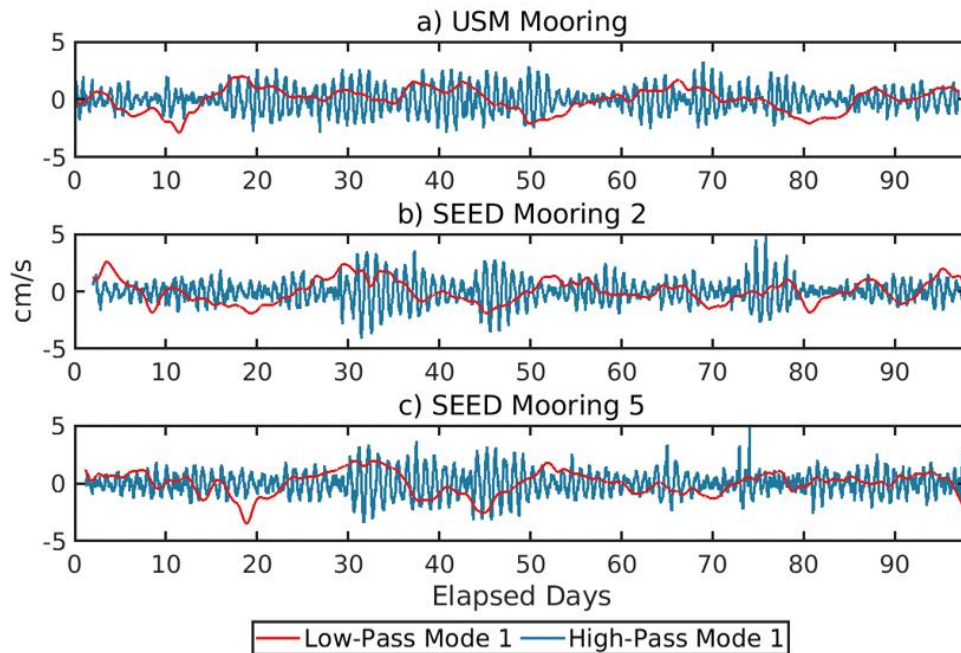
Figure 3.27 *Mode 1 Low-pass and High-pass u Time Components Across Shelf*

The time component of the mode 1 low-pass (red) and high-pass (blue) u velocities for the a) USM Mooring, b) SEED station 2, and

c) SEED station 5.

3.7 Forcing and Modulations of Inertial Motions

The motions in our high-pass time series are mostly associates with inertial

motions. Since these motions are created by the wind, they may be correlated with wind

stress and wind work. The wind stress also can create upwelling and downwelling which

can affect the stratification within the water column. If the stratification of the water

column is destroyed or subdued, then inertial oscillations can be shut down. In such

cases, the high-frequency kinetic energy will decrease as well. Since the high-frequency

kinetic energy is dominated by wind-induced near-inertial motions, we expect to see

increases in high-frequency kinetic energy during wind events. The goal of this section is

to determine if modulations in inertial kinetic energy can be correlated with wind stress

and wind work and with upwelling and downwelling. Upwelling and downwelling are

54

associated with the low-pass mode 1 u component. If the u component is negative (westward alongshore flow), we expect downwelling. If the u component is positive (eastward alongshore flow), we expect upwelling. The wind measurements are taken at different locations than the velocity measurements, and therefore we expect the correlation between the effect of wind and high-frequency kinetic energy not to be perfect. The wind stress, wind work, depth-averaged high-frequency kinetic energy, and EOF mode 1 for the low-pass u velocities are plotted in Figure 3.28 for the nearshore USM station, in Figure 3.29 for the mid-shelf SEED station 2, and in Figure 3.30 for the near shelf break SEED station 5.

None of the stations had available surface data, so the wind work was calculated using the shallowest available ADCP depth bin. For the nearshore and mid-shelf stations, this was within the top 5 m of the water column, however, at the near shelf break station, the shallowest depth was around 10 m. This data gap might skew the effect of wind work at these stations. Since the off-shelf thermocline occurs below 20 m in the northern Gulf of Mexico year-round (as shown in Figure 1.2), the near-surface measurements at the deeper SEED stations are still within the mixed layer. Table 2.1 shows the depth for the shallowest bin at all stations as well as the difference in depth between bins.
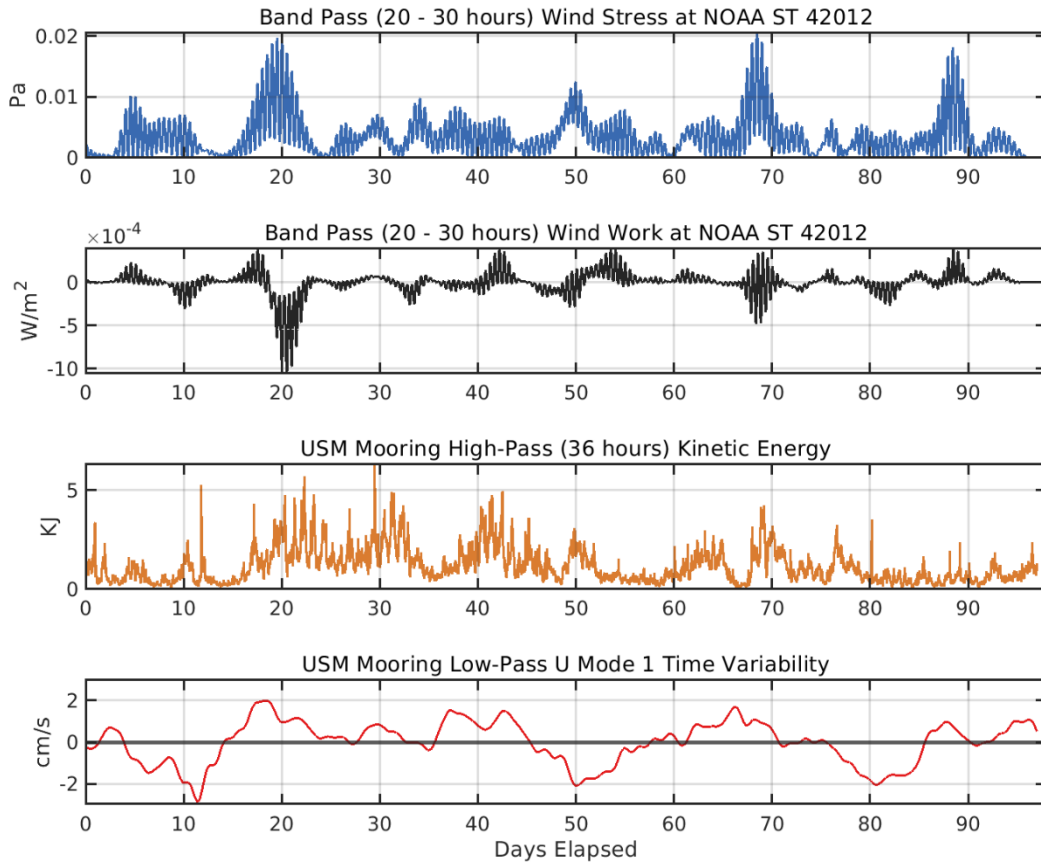
Figure 3.28 *Wind Stress, Wind Work, High-pass Kinetic Energy, and Low-pass u Mode 1 for USM Station*

The calculated wind stress, wind work, high-frequency kinetic energy, and low-pass u EOF mode 1 for the USM station using the wind data from NOAA Buoy Station 42012. The wind work and wind stress are velocities that are bandpassed between 20 and 30 hours to reduce noise.
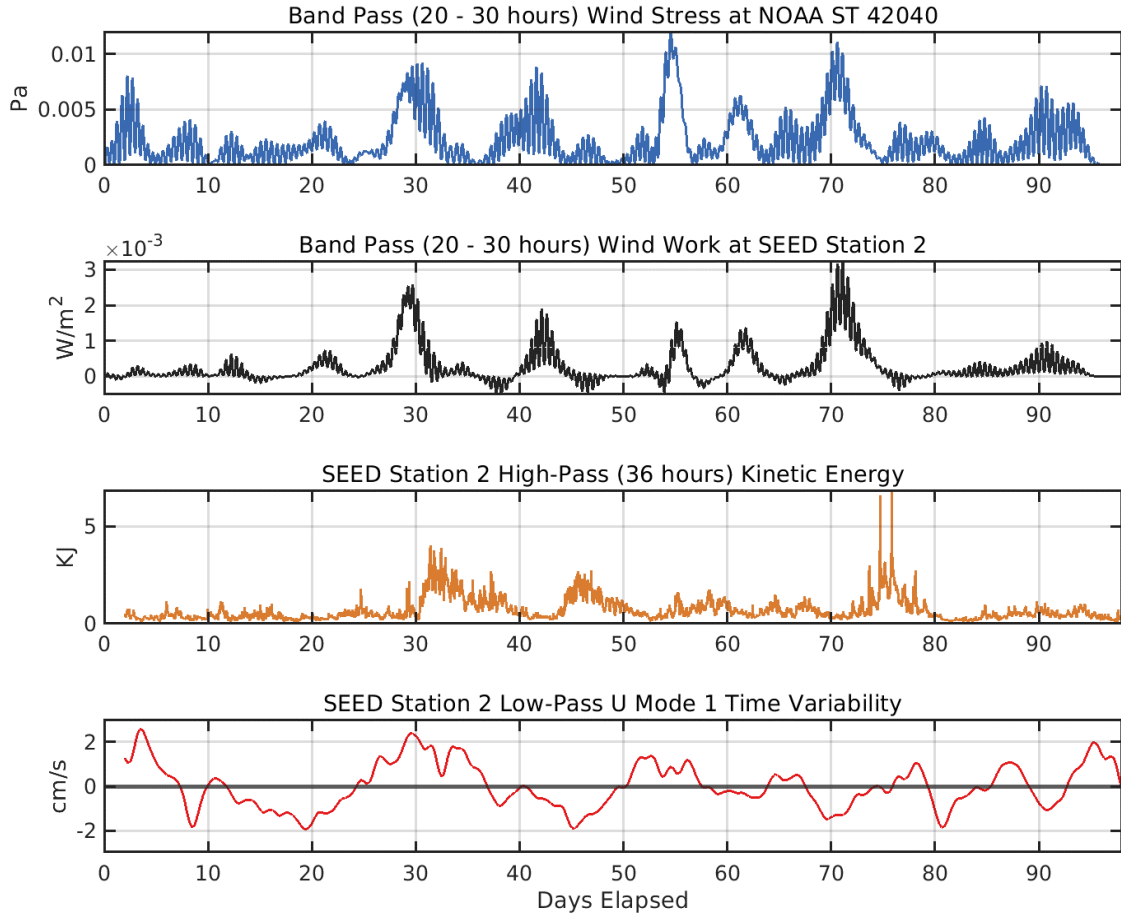
Figure 3.29 *Wind Stress, Wind Work, High-pass Kinetic Energy, and Low-pass u Mode 1 for SEED Station 2*

Same as Figure 3.28 but for SEED Station 2. Wind data was taken from NOAA Buoy Station 42040.
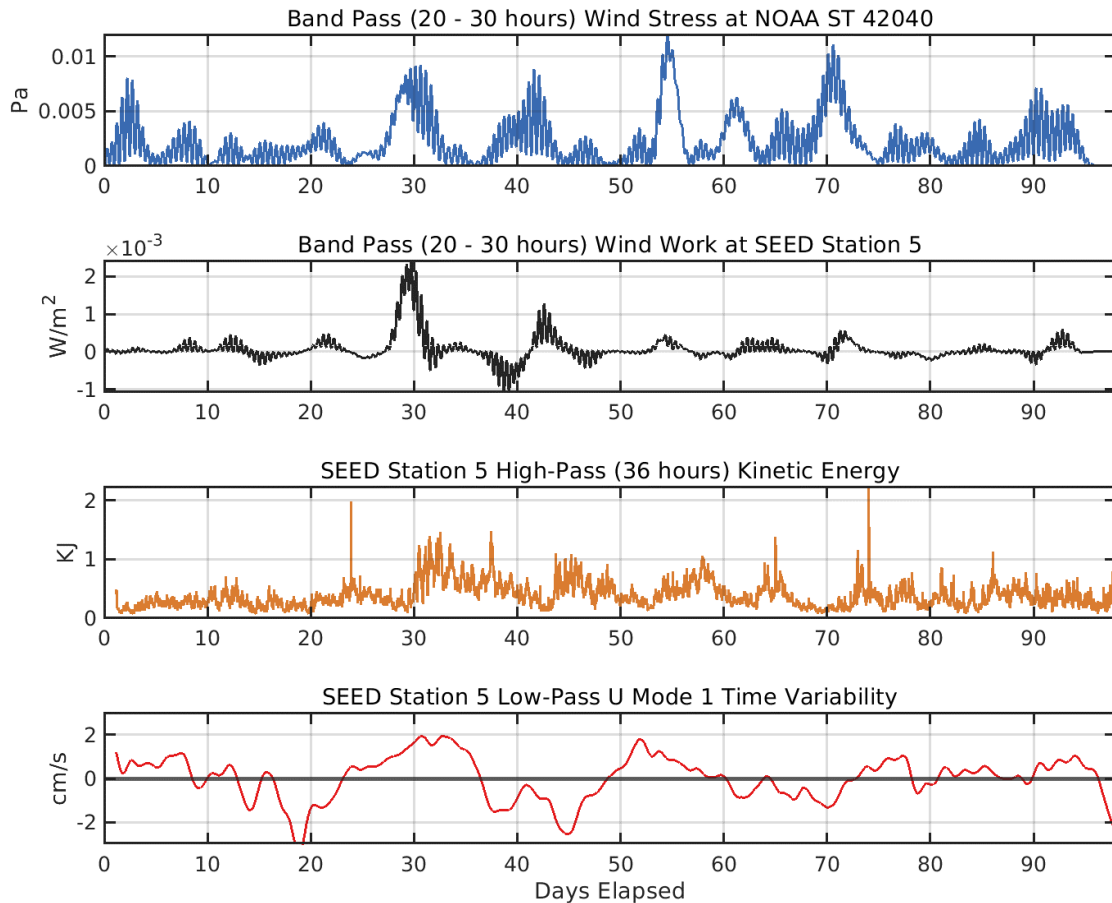
Figure 3.30 *Wind Stress, Wind Work, High-pass Kinetic Energy, and Low-pass u Mode 1 for SEED Station 5*

Same as Figure 3.28 but for SEED Station 5. Wind data was taken from NOAA Buoy Station 42040.

Within the nearshore mooring, some correlation between the mesoscale circulation and modulations of high-frequency kinetic energy can be seen. Downwelling at this station occurs between days 5 and 10, days 45 to 55, and days 75 to 85. During these times we either see an immediate weakening of kinetic energy or delayed weakening of kinetic energy. These events of downwelling are also visible in the CTD results in Figure 3.1. We also see increases in kinetic energy that are correlated with or near the times of increased wind stress and wind work during non-downwelling periods.

58

This is indicative that at the nearshore station, wind-induced near-inertial motions are present and are weakened by downwelling processes that reduce stratification.

Within the SEED stations, less correlation is found between the mesoscale circulation and high-frequency kinetic energy. In the mid-shelf stations, negative low-pass EOF mode 1 u velocities are found between days 10 and 25, days 40 to 50, days 70 to 75, and near days 80 and 90. At the near shelf break stations, negative low-pass EOF mode 1 u velocities are found between days 15 and 20, days 40 and 50, and days 60 and 70. However, unlike the nearshore stations, these do not always relate to downwelling events. At the mid-shelf stations, there are instances of sudden decreases of high-frequency kinetic energy during periods of negative low-pass EOF mode 1 u velocities, but there are also instances where high-frequency kinetic energy does not appear to be affected at all by the low-pass u velocities. At the near shelf break station, even less correlation is seen. While the lack of correlation at the deeper stations may be due to a data gap within the top 10 m of the water column, the shallowest ADCP bin is still within the mixed layer. Other processes, such as background vorticity time variability, may also affect the near-inertial energy fluctuations at the deeper stations.

At all stations, however, there are many instances of increased wind stress and wind work creating increased high-frequency kinetic energy. This suggests that across the shelf, near-inertial motions are present, but they are not actively suppressed by downwelling except at the nearshore station.

CHAPTER IV – DISCUSSION AND CONCLUSION

For this study, we analyzed data sets from three different isobaths on the Mississippi Shelf to gain a better insight into the motions across the shelf and how they interact. We were particularly interested in determining what motions are dominant, at what frequencies do these motions occur, what is their spatial variability and their vertical structure, and how are high-frequency motions modulated by the mesoscale motions.

When examining the kinetic energy, we found that the total energy decreases across the shelf towards the shore. We found that the barotropic energy across the shelf was mainly associated with low-frequency (mesoscale) motions. The barotropic motions are dominant near the shelf break. We found that the baroclinic kinetic energy is mainly governed by high-frequency motions across the shelf. Baroclinic motions are dominant near the shore and at the mid-shelf.

After performing a rotary spectral analysis, we found that a large broadband signal of clockwise rotating high-frequency energy is seen near the diurnal period (Figure 3.14, Figure 3.15, and Figure 3.16). Since the energy signal was broadband with peaks at different periods (Figure 3.17, Figure 3.18, and Figure 3.19), we conclude that tidal forcing is irrelevant. Instead, we argue that this peak in diurnal energy is due to near-inertial motions (see also Appendix A).

The existence of near-inertial waves in this area is further shown by the results of the harmonic analysis on the high-frequency motions (Figure 3.8, Figure 3.9, and Figure 3.10). These results show downward energy propagation with an upward phase which suggests internal waves. Diurnal internal tides will not propagate in this area. Semi-diurnal internal tides may propagate but they are much weaker than the diurnal motions.

Since these internal waves with diurnal frequencies cannot be internal tides and since the energy is seen propagating from the surface, we conclude that these motions are instead near-inertial motions that are projecting onto the tidal frequencies.

We performed an EOF analysis on both the low-frequency and high-frequency motions at each station on the shelf. For each station, the corresponding high-frequency u and v eigenfunctions were similar (Figure 3.20, Figure 3.22, and Figure 3.24). This further indicates the existence of near-inertial motions across the shelf.

The EOF analysis for the low-pass motions shows the downwelling phenomenon that modulates the inertial motions. Within the low-frequency eigenfunctions, vertical shear is seen in the mode 1 u velocities at the USM station (Figure 3.21a) but not at the deeper SEED stations (Figure 3.22a and Figure 3.24a). At the nearshore station, the low-frequency mode 1 v eigenfunction shows an out of phase motion between the surface and bottom (Figure 3.21b). The mid-shelf and near shelf break stations do not show an out of phase motion for mode 1 (Figure 3.23b and Figure 3.25b).

The connection between the low-pass alongshore velocity shear at the USM station and the upwelling and downwelling can be explained with the thermal wind balance equation (Pond and Pickard, 1995):

$$\frac{\partial u}{\partial z} = \frac{g}{\rho_0 f} \frac{\partial \rho}{\partial y} \tag{15}$$

in which z is the depth coordinate, g is the gravitational acceleration, ρ_0 is the reference density, f is the Coriolis force, ρ is density, u is the alongshore velocity, and y is the cross-shore coordinate. This equation shows the relation between horizontal density gradients $\frac{\partial \rho}{\partial y}$ and vertical velocity gradients $\frac{\partial u}{\partial z}$ (shear). For example, during eastward

alongshore flows, $\frac{\partial u}{\partial z} > 0$ and hence $\frac{\partial \rho}{\partial y} > 0$. This implies that the density of the water

will increase towards the shore. This would indicate upwelling as the denser bottom

water is moved up towards the shore while the surface water is pushed away from the

shore. During westward alongshore flows, $\frac{\partial u}{\partial z} < 0$ and $\frac{\partial \rho}{\partial y} < 0$. In this case, the density of

the water will decrease towards the shore. This would indicate downwelling as the less

dense surface water is pushed towards the shore where it piles up and is forced

downward, pushing the denser bottom water further offshore. Figure 4.1 presents a

schematic of how the vertical shear in the alongshore velocity relates to the upwelling

and downwelling at the USM station.
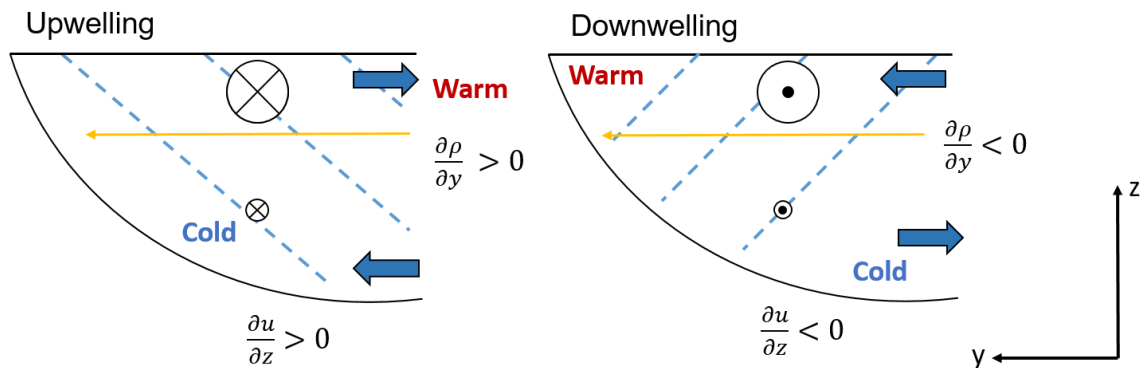
Figure 4.1 *Upwelling and Downwelling Vertical Shear Schematic*

The relation between the vertical shear in the alongshore velocity and the upwelling and downwelling processes at the USM mooring.

During upwelling and downwelling, the cross-shore surface and bottom velocities

are out of phase. This can be seen in the low-pass mode 1 *v* eigenfunction in Figure 3.21b

and its temporal variability in Figure 3.26. We conclude that upwelling and downwelling

processes are prevalent in the nearshore stations. Since no vertical shear in the low-

frequency *u* velocity and no out of phase low-frequency *v* motions are seen at the mid-

shelf and nearshore stations, we argue that these mesoscale processes are not dominant at these locations.

During downwelling events, the stratification is subdued near the surface at the USM station which in turn will modulate high-frequency motions such as near-inertial waves which rely on stratification to propagate. As such, in instances in which $\frac{\partial u}{\partial z} < 0$ a decrease in high-frequency kinetic energy will be seen. This can be seen in Figure 3.28 where instances of clear downwelling correlate with decreased high-frequency kinetic energy at the nearshore station. During these downwelling periods, we also see that increased wind stress and wind work do not significantly increase the high-frequency motions, further indicating that downwelling processes are subduing the stratification of the water column at the nearshore USM station.

At the deeper mid-shelf and near shelf break stations, a correlation between possible downwelling events and weakened high-frequency kinetic energy was not found (Figure 3.29 and Figure 3.30). While this may be because measurements near the surface for the deeper stations were not available, we expect that upwelling and downwelling processes are not prevalent in these areas as the low-frequency EOF modes (Figure 3.23 and Figure 3.25) are not in balance according to the thermal wind equation.

APPENDIX A – **EFFECT OF EPISODIC AND PHASE SHIFTED NIW ON FREQUENCY**

SPECTRA

In order to determine the cause of the broadband diurnal signal found in Section

3.5, separate experiments were conducted. Multiple artificial storms that created waves

resembling near-inertial waves were examined using an FFT to determine how the

change in their characteristics affects the results. These waves were generated with a

local inertial period of 24 hours. Three different wave experiments were conducted.

For the first experiment, a wave with a constant frequency of $\frac{1}{24\ hours}$ was created

that lasted the entire time period of 180 days. For the following two experiments, twelve

storm events were simulated over a 180-day period. Each storm event was given a

dampening period of 10 days in which they would slowly dissipate. The storm events

were randomly generated at some hour within the 180-day period. However, two

different start times were recorded for each storm: 1) a start time rounded down to start at

midnight of the closest day and 2) the randomly generated hour previously mentioned. In

the second experiment, the inertial waves will always be in phase while in the third

experiment, the inertial wave will have different phases. The FFT results of the

continuous wave, constant phase waves, and phase shifted waves can be seen in Figure

A.2. The FFT of the continues inertial wave shows a single narrow band energy peak at

the 1-day period (Figure A.2a).

In the second experiment, the random storm events cause a broadband peak

(Figure A.2b). Since the inertial waves are all in phase, a narrow-band peak is visible at 1

day. Once the waves are phase shifted (Figure A.3a), the FFT creates a broad energy

spectrum near the inertial period without a distinct peak. This phase shift occurs

naturally, as NIW are generated by wind and storm events that can occur at all times. We

hypothesize that the episodic storm events and the phase shifts are responsible for the

broadband energy spectrum seen in our FFT results in Figure 3.15, Figure 3.16, Figure

3.17, Figure 3.18, and Figure 3.19. The experiments were also duplicated with storms

having a random initial amplitude. However, the shape of the broadband energy peak was

not shown to be significantly affected by the changing initial amplitudes.
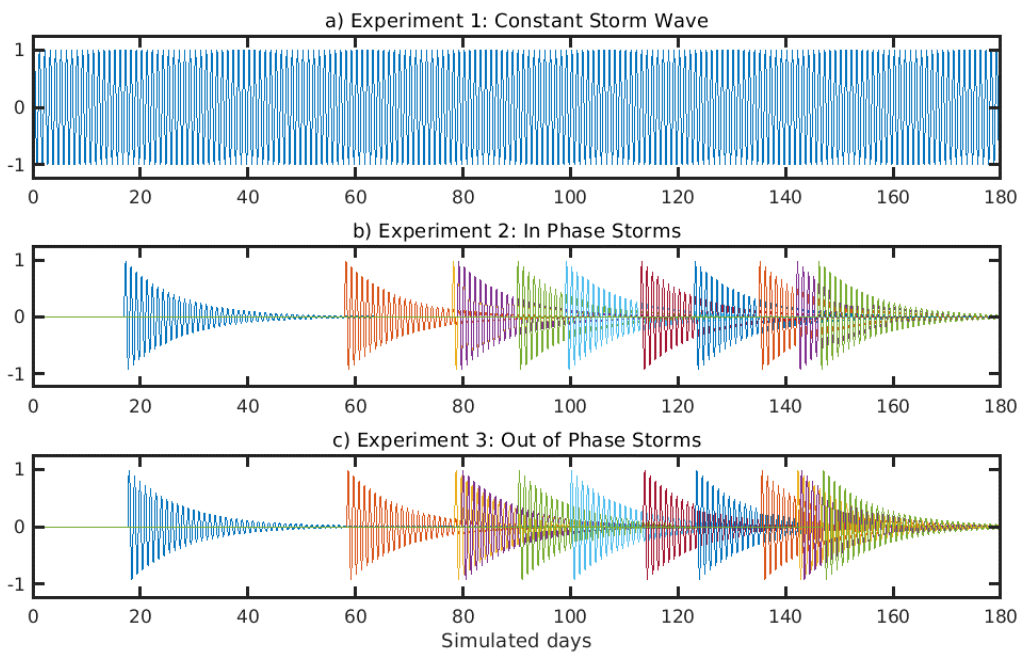
Figure A.1 *Simulated Storm Events Time Series*

The time series of the a) continuous wave with a 1-day period, b) randomly generated storm events with start times rounded down to

midnight for the corresponding day, and c) randomly generated storm events that are out of phase due to differing start hours.

Figure A.2 *FFT Results of Simulated Storm Experiments*

The FFT results of the time series shown in Figure A.1. a) Continuous storm wave, b) in phase storm waves, c) phase shifted storm

waves.

REFERENCES

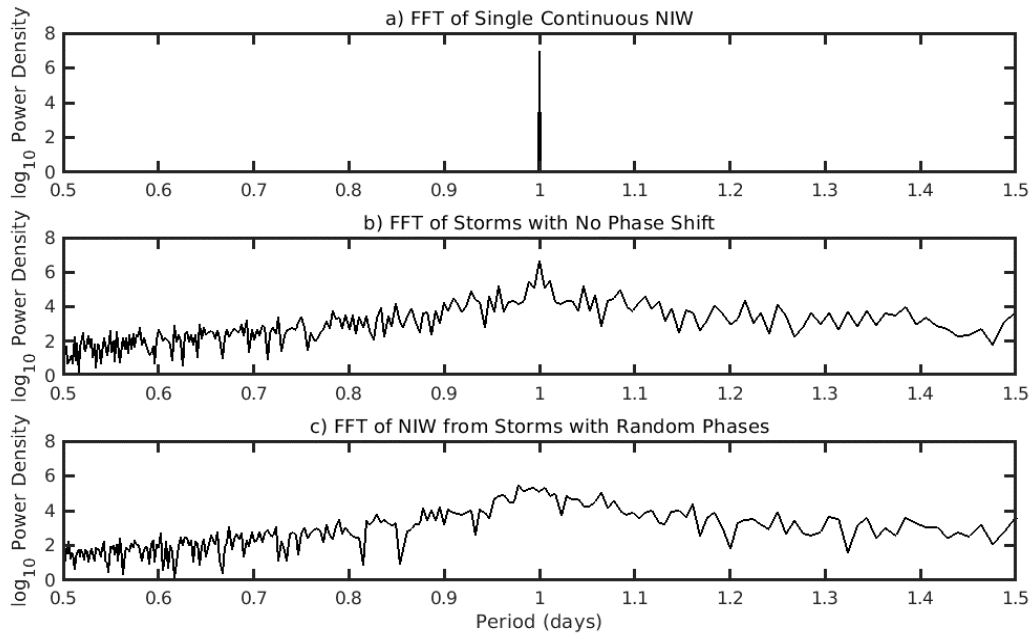Arnone, R., Vandermeulen, R., Donaghay, P., and Haoping, Y., 2016. Surface biomass flux across the coastal Mississippi shelf. *Ocean sensing and Monitoring VII, Proceedings of SPIE*, **Vol**. 9827, 1 – 9. https://doi.org/10.1117/12.2240874

Austin, J. A., and Lentz, S. J., 2002. The inner shelf response to wind-driven upwelling and downwelling, *J. Phys. Ocean*, **Vol. 32**, 2171 – 2193. https://doi.org/10.1175/1520-0485(2002)032<2171:TISRTW>2.0.CO;2

Buijsman, M. C., Arbic, B. K., Kelly, S. M., and Waterhouse, A. F., 2019. *Internal gravity waves*. Reference Module in Earth Systems and Environmental Sciences, Elsevier, https://doi.org/10.1016/b978-0-12-409548-9.04160-9

Bracco, A., Liu, G., and Sun, D., 2019. Mesoscale-submesoscale interactions in the Gulf of Mexico: from oil dispersion to climate. *Chaos, Solitons, and Fractals*, **Vol. 119**, 63 – 72. https://doi.org/10.1016/j.chaos.2018.12.012

Chen, C., Reid, R. O., and Nowlin, W. D. Jr., 1996. Near-inertial oscillations over the Texas-Louisana shelf. *J. Geophys. Res.*, **Vol. 101**, **No. C2**, 3509 – 3524. https://doi.org/10.1029/95JC03395

Chen, C., and Xie, L., 1997. A numerical study of wind-induced, near-inertial oscillations over the Texas-Louisiana shelf. *J. Geophys. Res.*, **Vol. 102**, **No. C7**, 15,583 – 15,593. https://doi.org/10.1029/97JC00228

Codiga, D. L., 2011. Unified Tidal Analysis and Prediction Using the UTide MATLAB Functions. Technical Report 2011, Graduate School of Oceanography, University of Rhode Island. 1 – 59.

Coogan, J., Dzwonkowski, B., and Lehrter, J., 2019. Effects of coastal upwelling and downwelling on hydrographic variability and dissolved oxygen in Mobile Bay. *J. Geophys. Res.*: Oceans, **Vol. 124**, 1 – 16. https://doi.org/10.1029/2018JC014592

DiMarco, S. F., Howard, M. K., and Reid, R. O., 2000. Seasonal variation of wind-driven diurnal current cycling on the Texas-Louisiana continental shelf. *Geophys. Res. Letters*, **Vol. 27, 7**, 1017 – 1020, https://doi.org/10.1029/1999GL010491

Dzwonkowski, B., and Park, K., 2010. Influence of wind stress and discharge on the mean and seasonal currents on the Alabama shelf of the northeastern Gulf of Mexico. *J. Geophys. Res.*, **Vol. 115**, **C12052**, 1 – 11. https://doi.org/10.1029/20101JC006449

Dzwonkowski, B., and Park, K., 2012. Subtidal circulation on the Alabama shelf during the Deepwater Horizon oil spill. *J. Geophys. Res.*, **Vol. 117**, 1 – 15. https://doi.org/10.1029/2011JC007664

Dzwonkowski, B., Greer, A., Briseno-Aveno, C., Kraise, J., Soto Ramos, I., Hernandez, F., Deary, A., Wiggert, J., Joung, D., Fitzpatrick, P., O'Brien, S., Dykstra, S., Lau, Y., Cambazoglu, M., Lockridge, G., Howden, S., Shiller, A., and Graham, W. M., 2017. Estuarine influence on biogeochemical properties on the Alabama shelf during the fall season. *Continental Shelf Res.*, **140(15)**, 96 – 109. https://doi.org/10.1016/j.csr.2017.05.001

Dzwonkowski, B., Fournier, S., Park, K., Dykstra, S., and Reager, J. T., 2018. Water column stability and the role of velocity shear on a seasonally stratified shelf, Mississippi Bight, northern Gulf of Mexico. *J. Geophys. Res.: Oceans*, **Vol. 123**, **8**, 5777 – 5796. https://doi.org/10.1029/2017JC013624

Emery, W. J., and Thomson, R. E., 2004. *Data Analysis Methods in Physical Oceanography: Second and Revised Edition*. Elsevier, 638 pp.

Foreman, M. G. G., and Henry, R. F., 1989. The harmonic analysis of tidal model time series. *Adv. Water Resources*, **Vol. 12**, 109 – 120. https://doi.org/10.1016/0309-1708(89)90017-1

Gerkema, T., and Zimmerman, J. T. F., 2008. *An Introduction to Internal Waves: Lecture Notes.* R. Neth. Inst. for Sea Res., Den Burg.

Gill, A. E., 1984. On the behavior of internal waves in the wakes of storms. *J. Phys. Oceanogr.,* **Vol. 14**, 1129 – 1151.

https://doi.org/10.1175/1520-0485(1984)014<1129:OTBOIW>2.0.CO;2

Gonella, J., 1972. A rotary-component method for analysing meteorological and oceanographic vector time series. *Deep Sea Res. and Oceanographic Abstracts*, **Vol. 19**, **12**, 833 – 846.

Gough, M. K., Reniers, A. J. H. M., MacMahan, J. H., and Howden, S. D., 2016. Resonant near-surface inertial oscillations in the northeastern Gulf of Mexico. *J. Geophys. Res.: Oceans*, **121**, 2163 – 2182, https://doi.org/10.1002/2015JC011372

Gouillon, F., Mory, S. L., Dukhovsky, D. S., and O'Brien, J. J., 2010. Forced tidal response in the Gulf of Mexico. *J. Geophys. Res.*, **Vol. 115**, **C10050**, 1 – 16, https://doi.org/10.1029/2010JC006122

Handley, L., Spear, K., Leggett, A., and Thatcher, C., 2012. Mississippi Sound: Chapter I, in *Emergent wetlands status and trends in the northern Gulf of Mexico: 1950 – 2010.* U.S. Geological Survey and U.S. Environmental Protection Agency. 1 – 16.

Hetland, R. D., and DiMarco, S. F., 2012. Skill assessment of a hydrodynamic model of circulation over the Texas-Louisiana shelf. *Ocean Modeling*, **Vol. 43 – 44**, 64 – 76. https://doi.org/10.1016/j.ocemod.2011.11.009

Hill, D. F., Griffiths, S. D., Peltier, W. R., Horton, B. P., and Törnqvist, T. E., 2011. High-resolution numerical modeling of tides in the western Atlantic, Gulf of Mexico, and Caribbean Sea during the Holocene. *J. Geophys. Res.*, **116**, **C10014**, 1 – 16. https://doi.org/10.2029/2010JC006896

Johnson, D. R., 2008. Ocean surface current climatology in the northern Gulf of Mexico. *Marine Fisheries Initiative (MARFIN),* Univ. of Southern Mississippi, Gulf Coast Research Lab, Ocean Springs, MS.

Kantha, L., 1998. Tides – a modern perspective. *Mar. Geodesy*, **21**, 275 – 297. https://doi.org/10.1080/01490419809388143

Kantha, L., 2005. Barotropic tides in the Gulf of Mexico. *Geophys. Monograph Ser.*, **161**, 159 – 163. https://doi.org/10.1029/161gm13

Knauss, J. A., and Garfield, N., 2017. *Introduction to Physical Oceanography: Third Edition.* Waveland Press, 310 pp.

Kundu, P. K., and Allen, J. S., 1976. Some three-dimensional characteristics of low-frequency current fluctuations near the Oregon coast. *J. Phys. Ocean.*, **Vol. 6**, 181 – 199. https://doi.org/10.1175/1520-0485(1976)006%3C0181:STDCOL%3E2.0.CO;2

Large, W. G., and Pond, S., 1980. Open ocean flux measurements in moderate to strong winds. *J. Phys. Ocean.*, **Vol. 11**, 3, 324 – 336. https://doi.org/10.1175/1520-0485(1981)011%3C0324:OOMFMI%3E2.0.CO;2

Liu, Y., Weisberg, R. H., Hu, C., Zheng, L., 2011. Tracking the Deepwater Horizon oil spill: a modeling perspective. *EOS Transactions AGU*, **Vol. 92**, 45 – 46. https://doi.org/10.1029/2011EO060001

Noble, M. A., and Ramp, S. R., 2000. Subtidal currents over the central California slope: evidence for offshore veering of the undercurrent and for direct, wind-driven slope currents. *Deep-Sea Res. Part II: Topical Studies in Oceanography*, **Vol. 47**, 871 – 906. https://doi.org/10.1016/S0967-0645(99)00130-7

Ohlmann, J. C., and Niiler, P. P., 2005. Circulation over the continental shelf in the northern Gulf of Mexico. *Prog. in Oceanog.*, **64**, 45 – 81. https://doi.org/10.1016/j.pocean.2005.002.001

Pond, S. and Pickard, G. L., 1995. *Introductory Dynamical Oceanography: Second Edition.* Butterworth Hinemann. 329 pp.

Price, J. F., Weller, R. A., and Schudlich, R. R., 1987. Wind-driven ocean currents and Ekman Transport. *Science, New Series*, **Vol. 238**, **No. 4833**, 1534 – 1538. https://doi.org/10.1126/science.238.4833.1534

Rippeth, T. P., 2005. Mixing in seasonally stratified shelf seas: a shifting paradigm. *Philos Trans A Math Phys Eng Sci*, **363(1837)**, 2837 – 2854. htpps://doi.org/10.1098/rsta.2005.1662

Seim, H. E., Kjerfve, B., and Sneed, J. E., 1987. Tides of the Mississippi Sound and the adjacent continental shelf. *Estuarine, Coastal, and Shelf Sci.,* **25**, 143 – 156.

Trenberth, K. E., Large, W. G., and Olson, J. G., 1989. The effective drag coefficient for evaluating wind stress over the oceans. *J. Climate.*, **Vol. 2**, 12, 1507 – 1516. https://doi.org/10.1175/1520-0442(1989)002%3C1507:TEDCFE%3E2.0.CO;2

Teague, W. J., Jarosz, E., Wang, D. W., and Mitchell, D. A., 2007. Observed oceanic

    response over the upper continental slope and outer shelf during Hurricane Ivan. *J.*

    Phys. Oceanogr., **Vol. 37**, 2181 – 2206. https://doi.org/10.1175/JPO3115.1

Walker, N. D., Wiseman, Jr., W. J., Rouse, Jr., L. J., and Babin, A., 2005. Effects of river

    discharge, wind stress, and slope eddies on circulation and the satellite-observed

    structure of the Mississippi River plume. *J. Coast. Res.*, **Vol. 21**, 6, 1228 – 1244.

    https://doi.org/10.2112/04-0347.1

Wang, D. W., Mitchell, D. A., Teague, W. J., Jarosz, E., and Hulbert, M. S., 2005.

    Extreme waves under Hurricane Ivan. *Science*. **Vol. 309**, 5736, 896.

    https://doi.org/10.1126/science.1112509

Zhai, X., Johnson, H. L., Marshall, D. P., and Wunsch, C., 2012. On the wind power

    input to the ocean general circulation. *J. Phys. Ocean*. **Vol. 42**, 8, 1357 – 1365.

    https://doi.org/10.1175/JPO-D-12-09.1.